

**Static analysis of shear flexible beams and frames  
in adhesive contact with an isotropic elastic half-plane  
using a coupled FE-BIE model**

Enrico TEZZON<sup>a</sup>, Nerio TULLINI<sup>b</sup>, Fabio MINGHINI<sup>c</sup>

*Department of Engineering, University of Ferrara, Via Saragat 1, Ferrara, Italy*

<sup>a</sup> e-mail: enrico.tezzon@unife.it

<sup>b</sup> Corresponding author. e-mail: nerio.tullini@unife.it

<sup>c</sup> e-mail: fabio.minghini@unife.it

**ABSTRACT**

Shear deformable beams and frames in perfect adhesion with an isotropic elastic half-space are analysed in plane strain or plain stress states. By means of a mixed variational formulation, the beam elements are described in terms of nodal displacements and rotations using locking-free shape functions, whereas the soil substrate is represented in terms of surface tractions through a boundary integral equation that incorporates a suitable Green's function. The formulation ensures full continuity between structure and substrate in terms of displacements and rotations.

A variety of numerical examples is presented to show the effectiveness of the proposed model. For very stiff beams subjected to a point force or moment, comparisons are made with available closed-form solutions to the contact problem of a rigid indenter. For foundation beams bonded to the substrate and loaded by a vertical point force the proposed model exhibits a superior convergence rate in comparison with other standard numerical models. Moreover, the shear deformations are shown to play a crucial role on both beam displacements and soil surface tractions. Finally, the soil-structure interaction analysis of a two-bay plane frame is presented.

*Keywords:* Soil-structure interaction; Plane strain; Plane stress; Two-dimensional half-space; Green's function; Mixed finite elements; Timoshenko beam; Locking-free finite element.

## 1 INTRODUCTION

The interest for contact problems and the analysis of the relevant interface reactions concern natural sciences, such as geology [1], as well as many engineering fields, such as aeronautics and space applications [2], structural strengthening of concrete with FRP composites [3, 4, 5], mechanical engineering [6, 7, 8] and electronics [9].

In the field of structural engineering, the assessment of the soil-structure interaction has been a challenge for a long time [10, 11]. Analytical solutions were restricted to rigid punches or infinite beams resting on isotropic or anisotropic elastic half-space [12, 13, 14]. Hence the adoption of simple soil models; in particular Winkler model, based on the proportionality between pressure and vertical displacements at every point of the contact surface, and the models introduced by Filonenko-Borodish and Pasternak, who assumed the existence of a shear layer lying on the top surface of the Winkler bed of linear springs [10]. Nevertheless, simplified substrate models like these should be restricted to problems in which the effects of transverse interaction between adjacent parts of the soil surface are not significant.

With regard to numerical methods, soil-structure interaction problems were studied with several approaches. In one approach, both the foundation beam and the substrate were described by means of the Finite Element Method (FEM) allowing for complex soil media and surface profiles [10]. However, to ensure vanishing displacements at the boundaries, the substrate mesh has to be extended far away from the loaded area, leading to a very large number of finite elements and to a discouraging computing time. To improve the computational efficiency, infinite elements were used, see [11] and references cited therein. It is worth observing that using classical beam theory and two-dimensional finite elements for the substrate does not allow for the angular continuity at the contact surface. In principle, this problem may be solved by introducing refined two-dimensional continuum elements containing rotational degrees of freedom [15].

In another approach, the behaviour of the soil medium is approximated by a proper soil model. The earliest applications of the elastic half-space model to soil-structure interaction problems were

due to Cheung and Zienkiewicz [16], and Cheung and Nag [17], who developed a model for the analysis of beams and plates resting on elastic foundations that incorporates Boussinesq's solution. Wang et al. [18] extended this procedure to the analysis of rigid pavements. Nevertheless, this method and many others adopting a similar approach (see [10, 11]) implicitly assume that the beam is connected to the substrate at equally spaced points through a finite number of pinned-clamped rigid links. Thus, no angular continuity between beam and substrate can be imposed. Moreover, this approach requires the explicit inversion of the substrate flexibility matrix. Variational formulations including a suitable Green's function of the substrate were first presented in [19, 20]. Bielak and Stephan [21] investigated the bending problem of beams on elastic soil using a Green's function descending from Boussinesq's influence function. In [22], the analysis of frames with rigid footings resting on an isotropic elastic half-space is reported, whereas Bode et al. [23] used Green's functions of the soil for the assessment of the soil-structure interaction in dynamics.

Finally, a particularly advantageous tool for reproducing the response of the elastic half-space is the Boundary Element Method (BEM), because only the boundary of the elastic substrate has to be discretized, see [24] and references cited therein. However, soil tractions are usually considered as nodal reactions in the FE model of the foundation beam and, once again, the rotation continuity between beam and substrate is neglected. In the general formulation of BEM dealing with elastic half-space, Mindlin's fundamental solution is usually adopted to obtain the displacement field due to a point force applied in the interior of a homogeneous three-dimensional elastic solid [25]. The particular problem discussed in the present paper refers to loads applied to the ground surface of a two-dimensional half-space in plane state. Consequently, Flamant' and Cerruti's solutions are the proper fundamental solutions to be used [12, 13].

In the present paper, a coupled Finite Element-Boundary Integral Equation (FE-BIE) model is used for the plane strain or plane stress analysis of beams and frames bonded to a homogeneous, linearly elastic and isotropic two-dimensional half-space. The model makes use of a standard, displacement-based numerical formulation for the beam, coupled with an integral equation for the

substrate boundary that includes a suitable Green's function of the substrate. The independent variables of the mixed formulation proposed are beam displacements and rotations, and soil surface tractions in tangential and normal directions. Only the beam in contact with the substrate boundary has to be discretized. In [26], an analogous mixed formulation was used for the analysis of Timoshenko beams in frictionless contact with the substrate, whereas in [27] structural elements with no bending stiffness, such as bars and thin coatings, were investigated. In [28] and [29], using Euler-Bernoulli and Timoshenko beam theory, respectively, the coupled FE-BIE method was applied to the buckling analysis of beams and frames in frictionless contact with the substrate. To the authors' knowledge, the present proposal to use the FE-BIE model for the plane strain or plane stress static analysis of shear deformable beams and frames in adhesive contact with the substrate represents a new contribution.

Differently from the formulations available in the literature (see for example [10, 16, 17]), the proposed model enforces the angular continuity between foundation beam and half-plane boundary at the node locations. Moreover, the proposed model involves symmetric soil matrices, whereas the classical FEM-BEM approach based on collocation BEM requires an additional computational effort to remedy the lack of symmetry of the BEM coefficient matrix. In the present approach the weakly singular BIE is evaluated analytically, so avoiding singular and hyper-singular integrals, that are the major concern of the classical BEM. Finally, the resolving matrix has dimensions proportional to the number of the foundation beam FEs. Conversely, in the standard FEM, a refined mesh requires a stiffness matrix with dimensions that are several times the square of the number of FEs used for the foundation beam. The advantages outlined result in accurate solutions at low computational cost.

Several numerical examples are presented. For very stiff beams subjected to a point force or moment, comparisons are made with available closed-form solutions to the contact problem of a rigid indenter. For a rigid punch loaded by a bending moment and a foundation beams bonded to the substrate and loaded by a vertical point force, the proposed model exhibits a superior convergence

rate with respect to other two standard numerical models: a standard FE model that uses two-dimensional elastic elements to describe the soil and the approach proposed by Cheung in [16, 17]. Moreover, the shear deformations are shown to play a crucial role on both beam displacements and soil surface tractions. Foundation beams loaded by a horizontal point force at midspan or at one end section as well as beams loaded by a bending moment at midspan are considered. Finally, the model is applied to the soil-structure interaction analysis of a double-cell tunnel subjected to gravity and lateral loads.

## 2 VARIATIONAL FORMULATION

A beam bonded to a two-dimensional semi-infinite substrate is referred to a Cartesian coordinate system  $(O; x, z)$ , where  $x$  coincides with the centroidal axis of the beam, and  $z$  is chosen in the downward transverse direction (Fig. 1a). The beam has length  $L$  and cross-section depth  $h$ . Thus, the half-plane boundary is located at  $z = h/2$ . Generalised plane stress or plane strain state can be considered in the present formulation. In the latter case, cross-section breadth  $b$  is assumed to be unitary for both the beam and the half-plane. Small displacements and infinitesimal strains are adopted in the analysis. Both the beam and the substrate are made of homogeneous, linearly elastic and isotropic materials. In the following, elastic constants  $E_b$ ,  $G_b$ , and  $\nu_b$  denote longitudinal and transverse elastic moduli, and Poisson's ratio of the beam, respectively, whereas  $E_s$  and  $\nu_s$  represent Young's modulus and Poisson's ratio of the substrate. The centroidal axis of the beam is subjected to distributions of horizontal and vertical loads  $p_x(x)$  and  $p_z(x)$ , and couples  $m(x)$  (Fig. 1b). Moreover, perfect adhesion is supposed between the beam and the half-plane boundary. This assumption involves the development of both interfacial shear tractions  $r_x(x)$  and vertical normal tractions  $r_z(x)$  along the contact region (Fig. 1b).

## 2.1 Total potential energy for the foundation beam

Assuming positive cross-section rotations  $\varphi$  in counter-clockwise direction, axial and transverse displacements for a Timoshenko beam can be written as:

$$u_{bx}(x, z) = u_{bx,0}(x) + \varphi(x) z, \quad u_{bz}(x, z) = u_z(x), \quad (1a, b)$$

where  $u_{bx,0}$  and  $u_z$  are the axial displacement of the centroidal beam axis and the vertical displacement of both the beam and the half-plane boundary, respectively. The horizontal displacement of the half-plane boundary is given by  $u_x(x) = u_{bx,0}(x) + \varphi(x) h/2$ .

Axial and shear strains in the beam are:

$$\varepsilon_b = u'_{bx,0} + \varphi' z, \quad \gamma_b = u'_z + \varphi, \quad (2a, b)$$

where a prime stands for differentiation with respect to  $x$ . Plane state assumption yields the following stress-strain relations:

$$\sigma_b = E_0 \varepsilon_b, \quad \tau_b = G_b \gamma_b, \quad (3a, b)$$

where  $E_0 = E_b$  or  $E_0 = E_b/(1-\nu_b^2)$  for generalised plane stress or plane strain state, respectively, and  $G_b = E_b/[2(1+\nu_b)]$ .

The elastic strain energy for a beam of length  $L$  is the sum of strain energies  $U_{\text{beam},a}$  and  $U_{\text{beam},b}$ , associated with axial strain (subscript  $a$ ) and bending and transverse shear strains (subscript  $b$ ).

Using strain components (2a,b) and constitutive laws (3a,b),  $U_{\text{beam},a}$  and  $U_{\text{beam},b}$  can be written as:

$$U_{\text{beam},a} = \frac{1}{2} \int_L E_0 A_b (u'_{bx,0})^2 dx, \quad (4a)$$

$$U_{\text{beam},b} = \frac{1}{2} \int_L [D_b (\varphi')^2 + k_b G_b A_b (u'_z + \varphi)^2] dx. \quad (4b)$$

where  $A_b = bh$  is the cross-sectional area,  $D_b = E_0 b h^3 / 12$  is the flexural rigidity and  $k_b$  is the shear correction factor [30, 31]:

$$k_b = \frac{5}{6 - \nu_b G_b / E_b}, \quad k_b = \frac{5}{6 - \nu_b (1 + \nu_b) G_b / E_b}, \quad (5)$$

for a plane stress or a plane strain state, respectively.

The total potential energy of the beam,  $\Pi_{\text{beam}} = \Pi_{\text{beam},a} + \Pi_{\text{beam},b}$ , is obtained from the strain energy contributions and the potential of the external loads, resulting in:

$$\Pi_{\text{beam},a} = U_{\text{beam},a} - b \int_L (p_x - r_x) u_{bx,0} dx, \quad (6a)$$

$$\Pi_{\text{beam},b} = U_{\text{beam},b} - b \int_L [(p_z - r_z) u_z + (m - r_x h/2) \phi] dx. \quad (6b)$$

## 2.2 Total potential energy for the substrate

The solutions to the two-dimensional problem for a homogeneous, linear elastic and isotropic half-plane loaded by a point force normal or tangential to its boundary are referred to as Flamant' and Cerruti's solutions, respectively [12, 13]. In particular, the surface displacement  $u_i(x)$ , with  $i = x, z$ , due to a point force  $P_i(\hat{x})$  applied to the half-plane boundary can be expressed in closed form as  $u_i(x) = g(x, \hat{x}) P_i(\hat{x})$  (Fig. 2), where Green's function  $g(x, \hat{x})$  is given by the following expression:

$$g(x, \hat{x}) = -\frac{2}{\pi E} \ln \frac{|x - \hat{x}|}{d}. \quad (7)$$

In Eq. (7),  $E = E_s$  or  $E = E_s/(1 - \nu_s^2)$  for a generalised plane stress or plane strain state, respectively, and  $d$  represents an arbitrary length related to a rigid-body displacement.

The horizontal and vertical displacements of a point of the half-plane boundary due to the combined action of interfacial shear tractions  $r_x$  and normal tractions  $r_z$  can be written as [12, 13]:

$$u_x(x) = \int_L g(x, \hat{x}) r_x(\hat{x}) d\hat{x} - \frac{c}{2E} \left[ \int_{x_0}^x r_z(\hat{x}) d\hat{x} - \int_x^{x_L} r_z(\hat{x}) d\hat{x} \right], \quad (8a)$$

$$u_z(x) = \int_L g(x, \hat{x}) r_z(\hat{x}) d\hat{x} + \frac{c}{2E} \left[ \int_{x_0}^x r_x(\hat{x}) d\hat{x} - \int_x^{x_L} r_x(\hat{x}) d\hat{x} \right], \quad (8b)$$

where  $x_0, x_L$  are the abscissas of the beam end sections, and  $c = 1 - \nu_s$  or  $c = (1 - 2\nu_s)/(1 - \nu_s)$  for a generalised plane stress or plane strain state, respectively.

Making use of the theorem of work and energy for exterior domains [32], it is possible to show that total potential energy  $\Pi_{\text{soil}}$  for the half-plane equals one half of the work of the external loads [26, 27], i.e.,

$$\Pi_{\text{soil}} = -\frac{b}{2} \int_L (r_x u_x + r_z u_z) dx. \quad (9)$$

Substituting Eqs. (8a, b) into Eq. (9) yields  $\Pi_{\text{soil}} = \Pi_{\text{soil},a} + \Pi_{\text{soil},b}$ , where

$$\Pi_{\text{soil},a} = -\frac{b}{2} \int_L r_x(x) dx \left\{ \int_L g(x, \hat{x}) r_x(\hat{x}) d\hat{x} - \frac{c}{2E} \left[ \int_{x_0}^x r_z(\hat{x}) d\hat{x} - \int_x^{x_L} r_z(\hat{x}) d\hat{x} \right] \right\}, \quad (10a)$$

$$\Pi_{\text{soil},b} = -\frac{b}{2} \int_L r_z(x) dx \left\{ \int_L g(x, \hat{x}) r_z(\hat{x}) d\hat{x} + \frac{c}{2E} \left[ \int_{x_0}^x r_x(\hat{x}) d\hat{x} - \int_x^{x_L} r_x(\hat{x}) d\hat{x} \right] \right\}. \quad (10b)$$

### 2.3 Total potential energy for the beam-substrate system

Making use of Eqs. (6) and (10), the total potential energy of the beam-substrate system turns out to be:

$$\Pi = \Pi_{\text{beam}} + \Pi_{\text{soil}} = \Pi_{\text{beam},a} + \Pi_{\text{beam},b} + \Pi_{\text{soil},a} + \Pi_{\text{soil},b}, \quad (11)$$

which is a mixed variational formulation with variational functions represented by displacements  $u_{bx,0}, u_z$  and rotation  $\phi$ , as well as interfacial shear and normal tractions  $r_x$  and  $r_z$  along the contact region. It is worth noting that using Green's function given by Eq. (7) reduces the domain of integration to the beam length only.

Several particular cases derive from Eq. (11). For instance, the frictionless interaction of a Timoshenko beam with the underlying substrate involves null interfacial shear traction  $r_x$  along the contact region. Accordingly, the displacement field in Eq. (8) reduces to



$$u_x(x) = -\frac{c}{2E} \left[ \int_{x_0}^x r_z(\hat{x}) d\hat{x} - \int_x^{x_L} r_z(\hat{x}) d\hat{x} \right], \quad (12a)$$

$$u_z(x) = \int_L g(x, \hat{x}) r_z(\hat{x}) d\hat{x}, \quad (12b)$$

and the total potential energy in Eq. (11) reduces to Eq. (13) reported in [26], where the mixed variational formulation is used to evaluate vertical displacement  $u_z$  and rotation  $\phi$  of the foundation beam, as well as contact pressure  $r_z$ .

Pressure  $r_z$  may be neglected when the bending stiffness of the beam is small, i.e., the beam is reduced to a thin coating. Consequently, only the interfacial shear traction  $r_x$  arises and the displacement field in Eq. (8) can be rewritten as

$$u_x(x) = \int_L g(x, \hat{x}) r_x(\hat{x}) d\hat{x}, \quad (13a)$$

$$u_z(x) = \frac{c}{2E} \left[ \int_{x_0}^x r_x(\hat{x}) d\hat{x} - \int_x^{x_L} r_x(\hat{x}) d\hat{x} \right], \quad (13b)$$

Moreover, the total potential energy in Eq. (11) reduces to Eq. (6) reported in [27], where the mixed variational formulation is used to evaluate both the axial displacement  $u_x$  of the thin coating and the interfacial shear traction  $r_x$ .

A stiff beam resting on a soft substrate behaves like a rigid indenter. Thus, the surface displacements are specified by the indenter profile and strain energies  $U_{\text{beam},a}$  and  $U_{\text{beam},b}$  in Eqs. (4) are equal to zero. Therefore, the total potential energy reduces to

$$\Pi = \Pi_{\text{soil},a} + \Pi_{\text{soil},b} - b \int_L [(p_x - r_x) \bar{u}_x + (p_z - r_z) \bar{u}_z + (m - r_x h/2) \bar{\phi}] dx \quad (14)$$

with  $\bar{u}_x$ ,  $\bar{u}_z$ , and  $\bar{\phi}$  being the prescribed tangential and normal displacements, and the prescribed rotation, respectively. With reference to the profile of a rigid flat indenter, the prescribed displacements are

$$\bar{u}_x(x) = u_{x,o}, \quad \bar{u}_z(x) = u_{z,o} - \phi_o x, \quad \bar{\phi}(x) = \phi_o \quad (15a, b, c)$$

where  $u_{x,o}$ ,  $u_{z,o}$ , and  $\varphi_o$  are specified at the origin  $x = z = 0$ . The variational principle (14) can be rewritten as

$$\Pi = \Pi_{\text{soil},a} + \Pi_{\text{soil},b} - b \left\{ u_{x,o} \int_L (p_x - r_x) dx + u_{z,o} \int_L (p_z - r_z) dx + \varphi_o \int_L [m - (p_z - r_z)x] dx \right\}. \quad (16)$$

It can readily be noted that, in Eq. (16), each integral in curly brackets imposes a global equilibrium equation.

With regard to an inextensible thin coating bonded to an elastic substrate, pressure  $r_z(x) = 0$  along the contact region, and variational principle (14) yields

$$\Pi = -\frac{b}{2} \int_L r_x(x) dx \int_L g(x, \hat{x}) r_x(\hat{x}) d\hat{x} - b \int_L (p_x - r_x) \bar{u}_x dx \quad (17)$$

Finally, for an indenter in frictionless contact with the substrate, the interfacial shear traction  $r_x = 0$  and Eq. (14) reduces to

$$\Pi = -\frac{b}{2} \int_L r_z(x) dx \int_L g(x, \hat{x}) r_z(\hat{x}) d\hat{x} - b \int_L [(p_z - r_z) \bar{u}_z + m \bar{\varphi}] dx \quad (18)$$

Variational forms similar to Eqs. (17) and (18) have widely been used to determine contact areas and pressures in contact problems involving rigid punches, see e.g. [19] and references cited therein.

### 3 FINITE ELEMENT MODEL

Both the foundation beam and the substrate boundary are subdivided into FEs. It is worth noting that the mesh of the half-plane boundary can be defined independently of that of the beam, but in the following the same mesh is adopted. The generic  $i$ th FE is characterised by initial and end coordinates  $x_i$  and  $x_{i+1}$ , length  $l_i = |x_{i+1} - x_i|$  and dimensionless local coordinate  $\xi = x/l_i$ . As usual in the FEM, vectors  $\mathbf{u}_{xi} = [u_{x,i}, u_{x,i+1}]^T$  and  $\mathbf{q}_{zi} = [u_{z,i}, \varphi_i, u_{z,i+1}, \varphi_{i+1}]^T$  of nodal displacements characterise the displacement field within the  $i$ th element by means of the following relations:

$$u(\xi) = \mathbf{N}_a(\xi) \mathbf{u}_{xi}, \quad [v(\xi), \varphi(\xi)]^T = \mathbf{N}_b(\xi) \mathbf{q}_{zi} \quad (19)$$

where vector  $\mathbf{N}_a(\xi)$  and matrix  $\mathbf{N}_b(\xi)$  contain the shape functions. In particular, for the analyses presented in the following,  $\mathbf{N}_a(\xi) = [N_{a,1}, N_{a,2}]$  collects linear Lagrangian functions  $N_{a,1} = 1 - \xi$  and  $N_{a,2} = \xi$ , whereas matrix  $\mathbf{N}_b(\xi)$  assembles “modified” Hermitian shape functions [26, 33-36]:

$$N_{b,11} = [1 - 3\xi^2 + 2\xi^3 + \phi_i(1 - \xi)]/(1 + \phi_i), \quad N_{b,12} = -l_i \xi [(1 - \xi)^2 + \phi_i(1 - \xi)/2]/(1 + \phi_i), \quad (20a, b)$$

$$N_{b,13} = [3\xi^2 - 2\xi^3 + \phi_i\xi]/(1 + \phi_i), \quad N_{b,14} = -l_i \xi [-\xi + \xi^2 - \phi_i(1 - \xi)/2]/(1 + \phi_i), \quad (20c, d)$$

$$N_{b,21} = 6\xi(1 - \xi)/[l_i(1 + \phi_i)], \quad N_{b,22} = [1 - 4\xi + 3\xi^2 + \phi_i(1 - \xi)]/(1 + \phi_i), \quad (20e, f)$$

$$N_{b,23} = -6\xi(1 - \xi)/[l_i(1 + \phi_i)], \quad N_{b,24} = (-2\xi + 3\xi^2 + \phi_i\xi)/(1 + \phi_i), \quad (20g, h)$$

where coefficient  $\phi_i = 12D_b/(k_b G_b A_b l_i^2)$ . Polynomials (20) follow from the exact solution to the homogeneous governing equations of Timoshenko beam theory [33]. Moreover, when shear deformations are negligible, coefficients  $\phi_i$  vanish and polynomials  $N_{b,1j}$  and  $N_{b,2j}$  ( $j = 1, \dots, 4$ ) in Eqs. (20) reduce to the classical Hermitian polynomials and to their first derivatives, respectively.

Soil reactions for the  $i$ th element can be approximated by the expressions:

$$r_x(\xi) = [\boldsymbol{\rho}_a(\xi)]^T \mathbf{r}_{xi}, \quad r_z(\xi) = [\boldsymbol{\rho}_b(\xi)]^T \mathbf{r}_{zi}, \quad (21a, b)$$

where  $\mathbf{r}_{xi}$ ,  $\mathbf{r}_{zi}$  denote nodal interfacial shear and normal tractions, respectively, and vectors  $\boldsymbol{\rho}_a$ ,  $\boldsymbol{\rho}_b$  collect constant or linear shape functions.

Substituting Eqs. (19), (21) into variational principle (11) and assembling over all elements, the potential energy takes the expression

$$\begin{aligned} \Pi(\mathbf{u}_x, \mathbf{q}_z, \mathbf{r}_x, \mathbf{r}_z) = & \frac{1}{2} \mathbf{u}_x^T \mathbf{K}_a \mathbf{u}_x + \frac{1}{2} \mathbf{q}_z^T \mathbf{K}_b \mathbf{q}_z - \mathbf{u}_x^T \mathbf{f}_x - \mathbf{q}_z^T \mathbf{f}_z + \mathbf{u}_x^T \mathbf{H}_{xx} \mathbf{r}_x + \mathbf{q}_z^T \mathbf{H}_{zz} \mathbf{r}_z + \mathbf{q}_z^T \mathbf{H}_{zx} \mathbf{r}_x \\ & - \frac{1}{2} \mathbf{r}_x^T \mathbf{G}_{xx} \mathbf{r}_x - \frac{1}{2} \mathbf{r}_z^T \mathbf{G}_{zz} \mathbf{r}_z - \frac{1}{2} \mathbf{r}_x^T \mathbf{G}_{xz} \mathbf{r}_z - \frac{1}{2} \mathbf{r}_z^T \mathbf{G}_{zx} \mathbf{r}_x \end{aligned} \quad (22)$$

where  $\mathbf{K}_a$ ,  $\mathbf{K}_b$  are the beam stiffness matrices and  $\mathbf{f}_x$ ,  $\mathbf{f}_z$  are the external load vectors, whose components for the  $i$ th FE can be written in the usual form:

$$k_{a,ij} = l_i \int_0^1 E_0 A_b(\xi) N'_{a,i}(\xi) N'_{a,j}(\xi) d\xi, \quad (23a)$$

$$k_{b,ij} = l_i \int_0^1 D_b(\xi) \left[ N'_{b,2i}(\xi) N'_{b,2j}(\xi) + \frac{12}{\phi_i l_i^2} (N'_{b,1i}(\xi) + N_{b,2i}(\xi))(N'_{b,1j}(\xi) + N_{b,2j}(\xi)) \right] d\xi, \quad (23b)$$

$$f_{x,i} = bl_i \int_0^1 N_{a,i}(\xi) p_x(\xi) d\xi, \quad (24a)$$

$$f_{z,i} = bl_i \int_0^1 N_{b,1i}(\xi) p_z(\xi) + N_{b,2i}(\xi) m(\xi) d\xi. \quad (24b)$$

With regard to the components of matrices  $\mathbf{H}_{xx}$ ,  $\mathbf{H}_{zz}$ ,  $\mathbf{H}_{xz}$  appearing in Eq. (22), the following expressions hold for the generic FE:

$$h_{xx,ij} = bl_i \int_0^1 N_{a,i}(\xi) \rho_{a,j}(\xi) d\xi, \quad (25a)$$

$$h_{zz,ij} = bl_i \int_0^1 N_{b,1i}(\xi) \rho_{b,j}(\xi) d\xi, \quad (25b)$$

$$h_{xz,ij} = \frac{bhl_i}{2} \int_0^1 N_{b,2i}(\xi) \rho_{a,j}(\xi) d\xi. \quad (25c)$$

Matrices  $\mathbf{G}_{xx}$ ,  $\mathbf{G}_{zz}$ ,  $\mathbf{G}_{xz}$ ,  $\mathbf{G}_{zx}$  are fully populated since they take account of the nonlocal relation between beam displacements and surface tractions. The components of these matrices are given by:

$$g_{xx,ij} = b \int_{x_i}^{x_{i+1}} \rho_{a,i}(x) dx \int_{x_j}^{x_{j+1}} g(x, \hat{x}) \rho_{a,j}(\hat{x}) d\hat{x}, \quad (26a)$$

$$g_{zz,ij} = b \int_{x_i}^{x_{i+1}} \rho_{b,i}(x) dx \int_{x_j}^{x_{j+1}} g(x, \hat{x}) \rho_{b,j}(\hat{x}) d\hat{x}, \quad (26b)$$

$$g_{xz,ij} = -\frac{bc}{2E} \int_{x_i}^{x_{i+1}} \rho_{a,i}(x) dx \left[ \int_{x_0}^x \rho_{b,j}(\hat{x}) d\hat{x} - \int_x^{x_L} \rho_{b,j}(\hat{x}) d\hat{x} \right], \quad (26c)$$

$$g_{zx,ij} = \frac{bc}{2E} \int_{x_i}^{x_{i+1}} \rho_{b,i}(x) dx \left[ \int_{x_0}^x \rho_{a,j}(\hat{x}) d\hat{x} - \int_x^{x_L} \rho_{a,j}(\hat{x}) d\hat{x} \right]. \quad (26d)$$

The integrals in Eqs. (26a, b) are weakly singular, i.e. they always exist in the Cauchy principal value sense and are finite. Moreover, if equal substrate shape functions are adopted, i.e.,  $\boldsymbol{\rho}_a = \boldsymbol{\rho}_b = \boldsymbol{\rho}$ , Eqs. (26a, b) involve symmetric matrices and yield  $\mathbf{G}_{xx} = \mathbf{G}_{zz}$ , whereas Eqs. (26c, d) imply the condition  $\mathbf{G}_{zx} = -\mathbf{G}_{xz}$ .

Requiring the total potential energy in Eq. (22) to be stationary, the following system of equations is obtained:

$$\begin{bmatrix} \mathbf{K} & \mathbf{H} \\ \mathbf{H}^T & -\mathbf{G} \end{bmatrix} \begin{Bmatrix} \mathbf{q} \\ \mathbf{r} \end{Bmatrix} = \begin{Bmatrix} \mathbf{f} \\ \mathbf{0} \end{Bmatrix}, \quad (27)$$

where

$$\mathbf{K} = \begin{bmatrix} \mathbf{K}_a & \mathbf{0} \\ \mathbf{0} & \mathbf{K}_b \end{bmatrix}, \quad \mathbf{H} = \begin{bmatrix} \mathbf{H}_{xx} & \mathbf{0} \\ \mathbf{H}_{xz} & \mathbf{H}_{zz} \end{bmatrix}, \quad \mathbf{G} = \begin{bmatrix} \mathbf{G}_{xx} & \mathbf{G}_{xz} \\ \mathbf{G}_{zx} & \mathbf{G}_{zz} \end{bmatrix}, \quad (28a, b, c)$$

$$\mathbf{q} = \begin{bmatrix} \mathbf{u}_x \\ \mathbf{q}_z \end{bmatrix}, \quad \mathbf{r} = \begin{bmatrix} \mathbf{r}_x \\ \mathbf{r}_z \end{bmatrix}, \quad \mathbf{f} = \begin{bmatrix} \mathbf{f}_x \\ \mathbf{f}_z \end{bmatrix}. \quad (29a, b, c)$$

Equation (27) represents the discrete system of equations governing the response of the beam-substrate system. From the numerical point of view, vectors  $\mathbf{q}$  and  $\mathbf{r}$  are obtained by solving Eq. (27). In particular, the following expressions hold:

$$\mathbf{r} = \mathbf{G}^{-1} \mathbf{H}^T \mathbf{q}, \quad (\mathbf{K} + \mathbf{K}_{\text{soil}}) \mathbf{q} = \mathbf{f}, \quad (30a, b)$$

where  $\mathbf{K}_{\text{soil}} = \mathbf{H} \mathbf{G}^{-1} \mathbf{H}^T$  is the stiffness matrix of the substrate. Some general considerations on stability and convergence properties of the proposed mixed FE model are reported in [26, 27], and references cited therein. Furthermore, it is simple to show that  $\mathbf{K}_{\text{soil}}$  is symmetric. In fact,  $(\mathbf{K}_{\text{soil}})^T = (\mathbf{H} \mathbf{G}^{-1} \mathbf{H}^T)^T = \mathbf{H} \mathbf{G}^{-T} \mathbf{H}^T = \mathbf{H} \mathbf{G}^{-1} \mathbf{H}^T = \mathbf{K}_{\text{soil}}$ , since matrix  $\mathbf{G}$  is symmetric, as it will be shown in Section 3.2.

It is worth noting that the second row of Eq. (27), containing the governing equation of the discrete Galerkin method for the system of Eqs. (8a, b), includes the beam rotations due to the

substrate tractions. In particular, the compatibility of rotation between foundation beam and soil substrate is enforced by the following term appearing in Eq. (6b):

$$-b \int_L [r_z u_z + r_x h/2 \phi] dx \quad (31)$$

leading to  $\mathbf{q}_z^T \mathbf{H}_{zz} \mathbf{r}_z + \mathbf{q}_z^T \mathbf{H}_{zx} \mathbf{r}_x$  in Eq. (22). Thus, matrices  $\mathbf{H}_{zz}$  and  $\mathbf{H}_{zx}$  play a key role in enforcing the compatibility of nodal rotations. It is also to be noted that the validity of Eq. (30a) does not depend on the presence of a foundation beam. In other words, Eq. (30a) may be used to obtain the surface tractions arising from a generic displacement field  $\mathbf{q}$  assigned to the half-plane boundary. The particular case of a flat rigid punch perfectly bonded to the substrate will be analysed in Sections 3.6 and 4.1.

Differently, Cheung and Nag [17], and many others adopting the same approach (see for example [11]), used Eqs. (8a, b) to compute the displacements due to piecewise constant soil tractions. This method implicitly assumes that the beam is connected to the substrate at equally spaced points through a finite number of pinned-clamped rigid links; thus, no angular continuity between beam and soil substrate can be imposed. Accordingly, the resulting soil matrix has to be augmented by rows and columns of zeros in correspondence of the nodal rotations. The numerical performance of the approach proposed in [17] is reported in Section 4.2.2 for comparison.

Finally, in the case of a structure connected to a foundation beam, Eq. (27) can be partitioned as reported in [26, 27]. In particular, denoting with  $\mathbf{q}_1$  and  $\mathbf{q}_2$  the vectors of nodal displacements referred to the structure only and those shared between structure and foundation beam, respectively, and with  $\mathbf{f}_1$  and  $\mathbf{f}_2$  the corresponding load vectors, Eq. (27) takes the form:

$$\begin{bmatrix} \mathbf{K}_{11} & \mathbf{K}_{12} & \mathbf{0} \\ \mathbf{K}_{21} & \mathbf{K}_{22} & \mathbf{H} \\ \mathbf{0} & \mathbf{H}^T & -\mathbf{G} \end{bmatrix} \begin{Bmatrix} \mathbf{q}_1 \\ \mathbf{q}_2 \\ \mathbf{r} \end{Bmatrix} = \begin{Bmatrix} \mathbf{f}_1 \\ \mathbf{f}_2 \\ \mathbf{0} \end{Bmatrix} \quad (32)$$

### 3.1 Prismatic beam subjected to uniform loads

For the sake of completeness, classical results referred to a prismatic beam subjected to uniform loads  $p_x(x)$ ,  $p_z(x)$  and couple  $m(x)$  are recalled. Beam stiffness matrices  $\mathbf{K}_a$ ,  $\mathbf{K}_b$  and external load vectors  $\mathbf{f}_x$ ,  $\mathbf{f}_z$  can be rewritten as

$$\mathbf{K}_a = \frac{E_0 A}{L} \tilde{\mathbf{K}}_a, \quad \mathbf{K}_b = \frac{D_b}{L^3} \tilde{\mathbf{K}}_b, \quad \mathbf{f}_a = b \tilde{\mathbf{f}}_a, \quad \mathbf{f}_b = b \tilde{\mathbf{f}}_b \quad (33a, b, c, d)$$

where, by virtue of Eqs. (23) and (24), the last terms on the right-hand sides are given by:

$$\tilde{\mathbf{K}}_{a,i} = \frac{L}{l_i} \begin{bmatrix} 1 & -1 \\ -1 & 1 \end{bmatrix}, \quad \tilde{\mathbf{f}}_{a,i} = \frac{p_x l_i}{2} \begin{bmatrix} 1 \\ 1 \end{bmatrix} \quad (34a, b)$$

$$\tilde{\mathbf{K}}_{b,i} = \frac{L^3}{(1+\phi_i)l_i^3} \begin{bmatrix} 12 & -6l_i & -12 & -6l_i \\ & (4+\phi_i)l_i^2 & 6l_i & (2-\phi_i)l_i^2 \\ & & 12 & 6l_i \\ \text{symm} & & & (4+\phi_i)l_i^2 \end{bmatrix} \quad (35a)$$

$$\tilde{\mathbf{f}}_{b,i} = p_z [l_i/2, -l_i^2/12, l_i/2, l_i^2/12]^T + m/(1+\phi_i) [1, l_i\phi_i/2, -1, l_i\phi_i/2]^T \quad (35b)$$

Assembly of global stiffness matrices  $\mathbf{K}_a$ ,  $\mathbf{K}_b$  and load vectors  $\mathbf{f}_a$ ,  $\mathbf{f}_b$  from the corresponding element matrices  $\mathbf{K}_{a,i}$ ,  $\mathbf{K}_{b,i}$  and load vectors  $\mathbf{f}_{a,i}$ ,  $\mathbf{f}_{b,i}$  follows the usual procedure. However, possible constraint equations among displacements or rotations of the foundation beam can be included into the total potential energy of the beam-substrate system (Eq. (22)) by means of a penalty approach, as illustrated in [28, 29].

### 3.2 Piecewise constant substrate tractions

In the following numerical examples, only piecewise constant functions are used to interpolate  $\mathbf{r}_x$  and  $\mathbf{r}_z$ , i.e., the shape functions for the soil tractions are assumed to be  $\rho_a(\xi) = \rho_b(\xi) = 1$ .

Consequently, matrices  $\mathbf{G}_{xx}$ ,  $\mathbf{G}_{zz}$ ,  $\mathbf{G}_{xz}$ ,  $\mathbf{G}_{zx}$  can be written as

$$\mathbf{G}_{xx} = \mathbf{G}_{zz} = \frac{b}{E} \tilde{\mathbf{G}}, \quad \mathbf{G}_{xz} = \frac{bc}{E} \tilde{\mathbf{G}}_{xz}, \quad (36a, b)$$

where the components of  $\tilde{\mathbf{G}}$  are given by:

$$\tilde{g}_{ii} = \frac{2l_i^2}{\pi} \left( \frac{3}{2} - \ln l_i \right) \quad (37a)$$

$$\tilde{g}_{ij} = \frac{2}{\pi} \left[ \frac{3}{2} l_i l_j + G(x_{j+1} - x_{i+1}) - G(x_{j+1} - x_i) - G(x_j - x_{i+1}) + G(x_j - x_i) \right] \quad \text{for } i \neq j \quad (37b)$$

In the previous equation  $G(x) = x^2/2 \ln|x|$  and parameter  $d$  has been omitted since a rigid-body displacement can be imposed in the post-processing analysis. The components of  $\tilde{\mathbf{G}}_{xz}$  are given by:

$$\tilde{g}_{xz} = \begin{cases} \tilde{g}_{xz,ij} = -l_i l_j / 2 & \text{if } i > j \\ \tilde{g}_{xz,ii} = 0 & \text{if } i = j \\ \tilde{g}_{xz,ij} = l_i l_j / 2 & \text{if } i < j \end{cases} \quad (38)$$

implying the property  $\mathbf{G}_{xz} = -\mathbf{G}_{xz}^T$ . Thus, taking into account that  $\mathbf{G}_{zx} = -\mathbf{G}_{xz}$ , the relation  $\mathbf{G}_{zx} = \mathbf{G}_{xz}^T$  is obtained. Therefore, matrix  $\mathbf{G}$  reported in Eq. (28c) is symmetric.

With regard to matrix  $\mathbf{H} = b \tilde{\mathbf{H}}$ , if piecewise constant tractions  $\mathbf{r}_x$  and  $\mathbf{r}_z$  are assumed, Eqs. (25) yield the following components for the  $i$ th FE

$$\tilde{\mathbf{h}}_{xx,i} = l_i / 2 [1, 1]^T \quad (39a)$$

$$\tilde{\mathbf{h}}_{zz,i} = [l_i / 2, -l_i^2 / 12, l_i / 2, l_i^2 / 12]^T \quad (39b)$$

$$\tilde{\mathbf{h}}_{xz,i} = \frac{h}{2(1 + \phi_i)} [1, \phi_i l_i / 2, -1, \phi_i l_i / 2]^T \quad (39c)$$

The  $i$ th column of global matrices  $\mathbf{H}_{xx}$ ,  $\mathbf{H}_{zz}$  and  $\mathbf{H}_{xz}$  contains only the vectors represented by Eqs. (39a), (39b) and (39c), respectively. Therefore, in a mesh with node and element numbers sorted in



ascending order and indicating with symbol '×' a nonzero entry, global matrices  $\mathbf{H}_{xx}$  and  $\mathbf{H}_{zz}$  are populated as follows:

$$\mathbf{H}_{xx} = \begin{bmatrix} \times & & & & \\ \times & \times & & & \\ & \times & \times & & \\ & & \times & \times & \\ & & & \times & \dots \end{bmatrix}, \quad \mathbf{H}_{zz} = \begin{bmatrix} \times & & & & \\ \times & & & & \\ \times & \times & & & \\ \times & \times & & & \\ & \times & \times & & \\ & \times & \dots & & \end{bmatrix}. \quad (40a, b)$$

Moreover, matrix  $\mathbf{H}_{xz}$  has nonzero entries in the same positions as  $\mathbf{H}_{zz}$ .

The foundation beam interposed between the substrate and the external load may be ignored if axial and bending beam stiffnesses are small. Consequently, beam matrix  $\mathbf{K}$  can be neglected in Eq. (27) and the corresponding equation,  $\mathbf{K}_{\text{soil}} \mathbf{q} = \mathbf{f}$ , gives the displacements of the soil surface due to assigned load distributions. As shown in [26] for flexible foundation beams in frictionless contact with the substrate, the vertical displacements of the soil surface are well approximated by the analytical solution resulting from the problem of an elastic half-plane loaded by a uniform vertical load  $p_z$ . However, Fig. 11d reported in [26] shows that pressure  $r_z$  may be affected by oscillations at the ends of the loaded region, similar to Gibbs oscillations in series analysis.

### 3.3 Prismatic beam with piecewise constant surface tractions

Making use of Eqs. (33) and (36), Eq. (27) may be rewritten as follows:

$$\begin{bmatrix} D_b/L^3 \tilde{\mathbf{K}} & b\tilde{\mathbf{H}} \\ b\tilde{\mathbf{H}}^T & -b/E\tilde{\mathbf{G}} \end{bmatrix} \begin{Bmatrix} \mathbf{q} \\ \mathbf{r} \end{Bmatrix} = \begin{Bmatrix} b\tilde{\mathbf{f}} \\ \mathbf{0} \end{Bmatrix}, \quad (41)$$

where

$$\tilde{\mathbf{K}} = \begin{bmatrix} \lambda_0^2 \tilde{\mathbf{K}}_a & \mathbf{0} \\ \mathbf{0} & \tilde{\mathbf{K}}_b \end{bmatrix}, \quad \tilde{\mathbf{H}} = \begin{bmatrix} \tilde{\mathbf{H}}_{xx} & \mathbf{0} \\ \tilde{\mathbf{H}}_{xz} & \tilde{\mathbf{H}}_{zz} \end{bmatrix}, \quad \tilde{\mathbf{G}} = \begin{bmatrix} \tilde{\mathbf{G}}_{xx} & c\tilde{\mathbf{G}}_{xz} \\ c\tilde{\mathbf{G}}_{xz}^T & \tilde{\mathbf{G}}_{zz} \end{bmatrix}, \quad \tilde{\mathbf{f}} = \begin{bmatrix} \tilde{\mathbf{f}}_x \\ \tilde{\mathbf{f}}_z \end{bmatrix}, \quad (42a, b, c, d)$$

with  $\lambda_0 = L/r_g$  and the radius of gyration  $r_g = h/\sqrt{12}$ . Therefore, solutions (30) reduce to

$$\mathbf{r} = E \tilde{\mathbf{G}}^{-1} \tilde{\mathbf{H}}^T \mathbf{q}, \quad D_b/L^3 [\tilde{\mathbf{K}} + (\alpha L)^3 \tilde{\mathbf{K}}_{\text{soil}}] \mathbf{q} = b \tilde{\mathbf{f}}, \quad (43a, b)$$

being  $\tilde{\mathbf{K}}_{\text{soil}} = \tilde{\mathbf{H}} \tilde{\mathbf{G}}^{-1} \tilde{\mathbf{H}}^T$  the nondimensional stiffness matrix of the substrate and

$$\alpha L = \sqrt[3]{b E L^3 / D_b}. \quad (44)$$

According to references [14, 26, 37], parameter  $\alpha L$  governs the static response of the beam-substrate system. Low values of  $\alpha L$  characterise short beams stiffer than soil, whereas high values of  $\alpha L$  correspond to slender beams on a relatively stiff soil. It is worth noting that a different parameter characterises the elastic response of a thin coating bonded to an elastic substrate. This parameter takes the following form [27, 38]:

$$\beta L = b E L / (E_0 A_b), \quad (45)$$

yielding the relationship  $(\alpha L)^3 = (\beta L) \lambda_0^2$ .

As stated above, mesh sizes of beam and substrate boundary can be defined independently of one another, and shape functions different from those of Eqs. (20) may be adopted as well. For example, in [27] quadratic Lagrangian bar elements including one or two equal substrate elements are used. In [26] beam-substrate matrices obtained using four equal soil elements for each beam element are reported.

### 3.4 Beam in frictionless contact with the substrate

For a beam resting in frictionless contact on an elastic half-plane,  $\mathbf{r}_x = \mathbf{f}_x = \mathbf{0}$ , and Eq. (27) reduces to the following expression:

$$\begin{bmatrix} \mathbf{K}_b & \mathbf{H}_{zz} \\ \mathbf{H}_{zz}^T & -\mathbf{G}_{zz} \end{bmatrix} \begin{Bmatrix} \mathbf{q}_z \\ \mathbf{r}_z \end{Bmatrix} = \begin{Bmatrix} \mathbf{f}_z \\ \mathbf{0} \end{Bmatrix} \quad (46)$$

coinciding with Eq. (26) reported in [26]. In particular, the second row of Eq. (46) contains the governing equation of the discrete Galerkin method for Eq. (12b), and relates beam rotations to

vertical reactions. Differently, in [16] a collocation method is proposed to solve Eq. (12b), but no angular continuity between the foundation beam and the substrate is ensured. Accordingly, static condensation was applied to beam matrix  $\mathbf{K}_b$ , so as to cancel out rows and columns corresponding to the nodal rotations.

The horizontal displacements at the substrate boundary may be obtained by making use of a Galerkin solution to Eq. (12a), written in the form:

$$\int_L r_z(x) u_x(x) dx = -\frac{c}{2E} \int_L r_z(x) dx \left[ \int_{x_0}^x r_z(\hat{x}) d\hat{x} - \int_x^{x_L} r_z(\hat{x}) d\hat{x} \right]. \quad (47)$$

The previous equation may be solved numerically using a piecewise constant discretization of both normal reactions  $r_z$ , see Eq. (21b), and horizontal displacements, i.e.,

$$u_x(\xi) = [\mathbf{p}_a(\xi)]^T \mathbf{u}_{xi}, \quad (48)$$

leading to the following expression:

$$\text{diag}(l_1, \dots, l_n) \mathbf{u}_x = \frac{c}{E} \tilde{\mathbf{G}}_{xz} \mathbf{r}_z. \quad (49)$$

### 3.5 Thin coating bonded to the substrate

With regard to a bar with zero bending stiffness (i.e., a thin coating) bonded to an elastic half-plane and having the centroidal axis coinciding with the substrate boundary,  $\mathbf{r}_z = \mathbf{f}_z = \mathbf{0}$ ,  $D_b = 0$ , and Eq. (27) reduces to the following expression (see Eq. (14) reported in [27]):

$$\begin{bmatrix} \mathbf{K}_a & \mathbf{H}_{xx} \\ \mathbf{H}_{xx}^T & -\mathbf{G}_{xx} \end{bmatrix} \begin{Bmatrix} \mathbf{q}_x \\ \mathbf{r}_x \end{Bmatrix} = \begin{Bmatrix} \mathbf{f}_x \\ \mathbf{0} \end{Bmatrix} \quad (50)$$

The vertical displacements at the substrate boundary may be obtained by making use of a Galerkin solution to Eq. (13b), written in the form:

$$\int_L r_x(x) u_z(x) dx = \frac{c}{2E} \int_L r_x(x) dx \left[ \int_{x_0}^x r_x(\hat{x}) d\hat{x} - \int_x^{x_L} r_x(\hat{x}) d\hat{x} \right]. \quad (51)$$

The previous equation may be solved numerically using a piecewise constant discretization of both tangential reactions  $r_x$ , see Eq. (21a), and vertical displacements, i.e.,

$$v(\xi) = [\boldsymbol{\rho}_a(\xi)]^T \mathbf{u}_{zi}, \quad (52)$$

leading to the following expression:

$$\text{diag}(l_1, \dots, l_n) \mathbf{u}_z = \frac{c}{E} \tilde{\mathbf{G}}_{zx} \mathbf{r}_x. \quad (53)$$

### 3.6 Rigid flat punch with piecewise constant surface tractions

Eq. (15) shows that vector  $\mathbf{q}_o = [u_{x,o}, u_{z,o}, \varphi_o]^T$ , collecting the displacements prescribed at the origin, governs the displacement field generated by a rigid flat punch. Thus, substituting Eqs. (21) into variational principle (16), assembling over all substrate elements, and requiring the potential energy to be stationary, the following system of equations is obtained

$$\begin{bmatrix} \mathbf{0} & \mathbf{H}_o \\ \mathbf{H}_o^T & -\mathbf{G} \end{bmatrix} \begin{Bmatrix} \mathbf{q}_o \\ \mathbf{r} \end{Bmatrix} = \begin{Bmatrix} \mathbf{f}_o \\ \mathbf{0} \end{Bmatrix}, \quad (54)$$

where

$$\mathbf{H}_o = \begin{bmatrix} \mathbf{h}_{o,xx}^T & \mathbf{0} \\ \mathbf{0} & \mathbf{h}_{o,zz}^T \\ \mathbf{0} & \mathbf{h}_{o,\varphi z}^T \end{bmatrix}, \quad \mathbf{f}_o = \begin{bmatrix} P_{x,o} \\ P_{z,o} \\ M_o \end{bmatrix}, \quad (55a, b)$$

vector  $\mathbf{f}_o$  collects the three external load resultants

$$P_{x,o} = \int_L p_x dx, \quad P_{z,o} = \int_L p_z dx, \quad M_o = \int_L (m - p_z x) dx, \quad (56a, b, c)$$

whereas vectors  $\mathbf{h}_{o,xx}$ ,  $\mathbf{h}_{o,zz}$ ,  $\mathbf{h}_{o,\varphi z}$  have the following components

$$h_{o,xx,i} = bl_i \int_0^1 \rho_{a,i}(\xi) d\xi, \quad h_{o,zz,i} = bl_i \int_0^1 \rho_{b,i}(\xi) d\xi, \quad h_{o,\varphi z,i} = -b \int_{x_i}^{x_{i+1}} \rho_{b,i}(x) x dx \quad (57a, b, c)$$

Assuming constant functions  $\rho_{a,i} = \rho_{b,i} = 1$ , Eqs. (57) reduces to

$$h_{o,xx,i} = h_{o,zz,i} = bl_i, \quad h_{o,\varphi z,i} = -bl_i \frac{x_i + x_{i+1}}{2}. \quad (58a, b, c,)$$

The first relation of Eq. (54),  $\mathbf{H}_o \mathbf{r} = \mathbf{f}_o$ , imposes equilibrium conditions between  $\mathbf{r}$  and  $\mathbf{f}_o$ , whereas the second relation,  $\mathbf{G} \mathbf{r} = \mathbf{H}_o^T \mathbf{q}_o$ , represents the governing equation of the discrete Galerkin method for the system of equations (8a, b), with displacements prescribed by Eqs. (15a, b). Moreover, the solutions to Eq. (54):

$$\mathbf{r} = \mathbf{G}^{-1} \mathbf{H}_o^T \mathbf{q}_o, \quad \mathbf{K}_o \mathbf{q}_o = \mathbf{f}_o, \quad (59a, b)$$

are similar to Eqs. (30a, b), with the only difference that the stiffness matrix of the substrate,  $\mathbf{K}_o = \mathbf{H}_o \mathbf{G}^{-1} \mathbf{H}_o^T$ , is a 3-by-3 matrix.

For an inextensible thin coating bonded to an elastic substrate, pressure  $r_z = 0$  along the contact region, the variational principle of Eq. (17) applies, and in Eq. (54) the following relations hold:

$\mathbf{G} = \mathbf{G}_{xx}$ ,  $\mathbf{H}_o = \mathbf{h}_{o,xx}^T$ ,  $\mathbf{q}_o = u_{x,o}$ ,  $\mathbf{r} = \mathbf{r}_x$ ,  $\mathbf{f}_o = P_{x,o}$ . Consequently, Eqs. (59) reduce to

$$\mathbf{G}_{xx} \mathbf{r}_x = u_{x,o} \mathbf{h}_{o,xx}, \quad u_{x,o} = P_{x,o}/k_{o,xx}, \quad (60a, b)$$

where  $k_{o,xx} = \mathbf{h}_{o,xx}^T \mathbf{G}_{xx}^{-1} \mathbf{h}_{o,xx}$ , and Eq. (60a) represents the governing equation of the discrete Galerkin method for first kind integral equations with a logarithmic kernel, see [39, 40] and references cited therein. As shown in [27], a thin coating bonded to a substrate behaves like an inextensible stiffener for  $\beta L < 0.5$ .

For the contact of a frictionless indenter, interfacial shear traction  $r_x = 0$ , the variational principle of Eq. (18) applies, and Eq. (54) reduces to

$$\begin{bmatrix} 0 & 0 & \mathbf{h}_{o,zz}^T \\ 0 & 0 & \mathbf{h}_{o,\varphi z}^T \\ \mathbf{h}_{o,zz} & \mathbf{h}_{o,\varphi z} & \mathbf{G}_{zz} \end{bmatrix} \begin{Bmatrix} u_{z,o} \\ \boldsymbol{\varphi}_o \\ \mathbf{r}_z \end{Bmatrix} = \begin{Bmatrix} P_{z,o} \\ M_o \\ \mathbf{0} \end{Bmatrix} \quad (61)$$

As shown in [26], a foundation beam in frictionless contact with the substrate behaves like a rigid punch for  $\alpha L < 1$ .

### 3.7 Prismatic beam-column with a rigid foundation placed at the bottom

For a prismatic beam-column element with the bottom node connected with the upper side of a rigid foundation beam of height  $h$  (node  $i$  in Fig. 3), a classical transformation matrix  $\mathbf{T}$  has to be adopted to impose the kinematical constraints between the degrees of freedom at node  $i$  and those at the substrate boundary (node  $o$  in Fig. 3):

$$\mathbf{q}_i = \mathbf{T}\mathbf{q}_{i,o} \Leftrightarrow \begin{bmatrix} u_{x,i} \\ u_{x,i+1} \\ u_{z,i} \\ \Phi_i \\ u_{z,i+1} \\ \Phi_{i+1} \end{bmatrix} = \begin{bmatrix} 1 & & & & & \\ & 1 & & & & \\ & & 1 & & & \\ & & & 1 & & \\ & & & & 1 & \\ & & & & & 1 \end{bmatrix} \begin{bmatrix} u_{x,o} \\ u_{x,i+1} \\ u_{z,o} \\ \Phi_o \\ u_{z,i+1} \\ \Phi_{i+1} \end{bmatrix}, \quad (62)$$

where unspecified entries in Eq. (62) are set equal to zero. The corresponding stiffness matrix and load vector for the  $i$ th element undergo the usual transformation rule, i.e.,  $\mathbf{K}_{i,o} = \mathbf{T}^T \mathbf{K}_i \mathbf{T}$  and  $\mathbf{f}_{i,o} = \mathbf{T}^T \mathbf{f}_i$ , whereas matrix  $\mathbf{H}_i$  of the element must be modified as

$$\mathbf{H}_i = \begin{bmatrix} \mathbf{h}_{o,xx}^T & \mathbf{0} \\ \mathbf{0} & \mathbf{0} \\ \mathbf{0} & \mathbf{h}_{o,zz}^T \\ \mathbf{0} & \mathbf{h}_{o,\varphi z}^T \\ \mathbf{0} & \mathbf{0} \\ \mathbf{0} & \mathbf{0} \end{bmatrix}. \quad (63)$$

## 4 NUMERICAL EXAMPLES

### 4.1 Rigid punch

Accuracy and convergence properties of the proposed coupled FE-BIE formulation are first evaluated with regard to the rotation of a rigid punch of length  $L$ , bonded to an elastic half-plane and subjected to a horizontal force  $P_x$  or to a bending moment  $M$ . Analytical solutions to these problems are available in the literature. In particular, the punch rotation can be written in closed form as [13]:

$$\varphi_P = \frac{(\kappa+1)\ln \kappa}{G(\pi^2 + \ln^2 \kappa)L} P_x \quad (64a)$$

$$\varphi_M = \frac{\pi(\kappa+1)}{2G(\pi^2 + \ln^2 \kappa)L^2} M \quad (64b)$$

for the case of horizontal force  $P_x$ , and for that of bending moment  $M$ , respectively. In the previous equations,  $\kappa = (3 - \nu_s)/(1 + \nu_s)$  for generalised plane stress state and  $\kappa = 3 - 4\nu_s$  for generalised plane strain state, and  $G = E_s/[2(1 + \nu_s)]$ .

For comparison purposes, both uniform and graded meshes are considered. Coordinate  $x_j$  of the generic  $j$ th node of the mesh is then given by:

$$x_j = \begin{cases} \frac{1}{2} \left[ \left( \frac{2j}{n_{el}} \right)^{\beta_{exp}} - 1 \right] & \text{if } 0 \leq j \leq n_{el}/2 \\ -x_{n_{el}-j} & \text{if } n_{el}/2 < j \leq n_{el} \end{cases} \quad (65)$$

with  $n_{el}$  being the total number of FEs in the mesh and  $\beta_{exp}$  the so-called grading exponent [41]. A uniform mesh is obtained by assuming  $\beta_{exp} = 1$ .

Figure 4a shows relative error  $e_{P\varphi} = |P_x/\varphi_P - P_x/\varphi_o|/(P_x/\varphi_P)$  versus  $n_{el}$  for  $\beta_{exp} = 1, 2, 3$ , where  $\varphi_o$  is the punch rotation obtained from the present analysis when the punch is subjected to force  $P_x$ . Analogously, Fig. 4b shows relative error  $e_{M\varphi} = |M/\varphi_M - M/\varphi_o|/(M/\varphi_M)$  versus  $n_{el}$  for  $\beta_{exp} = 1, 2, 3$ , where  $\varphi_o$  is the punch rotation obtained from the present analysis when the punch is subjected to moment  $M$ . In evaluating  $\varphi_P$  and  $\varphi_M$  from Eqs. (64),  $\kappa = 2.333$  is assumed. In Figs. (4a, b), relative errors decrease at a rate  $n_{el}^{-1.0}$  for uniform mesh ( $\beta_{exp} = 1$ ), and at higher rates, equal to  $n_{el}^{-2.0}$  and  $n_{el}^{-2.8}$ , for graded mesh with  $\beta_{exp} = 2$  and 3. In particular, for a uniform mesh with  $n_{el}$  greater than 32, relative error  $e_{P\varphi}$  is less than 1%, but the same error can be obtained with graded meshes having  $n_{el} \geq 8$ . Furthermore, relative error  $e_{M\varphi}$  is equal to 0.8% for a uniform mesh with  $n_{el} = 64$ , and  $e_{M\varphi}$  reduces to 0.4% for  $\beta_{exp} = 2$  and  $n_{el} = 16$ , or to 0.5% for  $\beta_{exp} = 3$  and  $n_{el} = 8$ .

Interfacial shear and normal tractions  $r_x(x)$  and  $r_z(x)$  for a rigid flat punch loaded by a horizontal force  $P_x$  and a vertical force  $P_z$  are given by Abramov's formulas [12, 13]:

$$r_x(x) = \frac{P_x c(x) + P_z s(x)}{2\pi\sqrt{(L/2)^2 - x^2}} \quad (66a)$$

$$r_z(x) = \frac{-P_x s(x) + P_z c(x)}{2\pi\sqrt{(L/2)^2 - x^2}} \quad (66b)$$

where  $c(x) = \frac{1+\kappa}{\sqrt{\kappa}} \cos\left(\frac{\ln \kappa}{2\pi} \ln \frac{L/2+x}{L/2-x}\right)$ ,  $s(x) = \frac{1+\kappa}{\sqrt{\kappa}} \sin\left(\frac{\ln \kappa}{2\pi} \ln \frac{L/2+x}{L/2-x}\right)$  and  $\kappa$  takes the

alternative expressions reported above. It is possible to show that the tractions obtained from Eqs. (66a, b) fluctuate in sign an infinite number of times as  $x$  tends to  $L/2$  [12]. However, for  $P_x = 0$  and  $\nu_s = 0.2$ , surface tractions become negative for the first time when  $x = +0.499996 L$ , which is so close to the edge of the punch that usual continuum mechanics hypothesis does not hold anymore.

In the case of a rigid flat punch subjected to a bending moment  $M$ , surface tractions  $r_x(x)$  and  $r_z(x)$  may be written in closed form as [12, 13]:

$$r_x(x) = \frac{M[\pi x s(x) - L(\ln \kappa) c(x)/2]}{(\pi^2 + \ln^2 \kappa)(L/2)^2 \sqrt{(L/2)^2 - x^2}} \quad (67a)$$

$$r_z(x) = \frac{M[\pi x c(x) + L(\ln \kappa) s(x)/2]}{(\pi^2 + \ln^2 \kappa)(L/2)^2 \sqrt{(L/2)^2 - x^2}} \quad (67b)$$

with  $c$ ,  $s$  and  $\kappa$  being obtained from the previously reported expressions.

The results in terms of surface tractions  $r_x$  and  $r_z$  obtained from the proposed FE-BIE formulation using a uniform mesh with  $n_{el} = 512$  substantially coincide with the analytical solutions of Eqs. (66) and (67). To evaluate the accuracy of numerical solutions obtained using a coarser FE discretization, horizontal and vertical reactions  $r_x$  and  $r_z$  between a rigid punch subjected to a vertical force  $P_z$  and the substrate are estimated by means of a graded mesh with  $n_{el} = 8$  and  $\beta_{exp} = 2$ . The results are reported in nondimensional form in Fig. 5 versus the relative position  $x/L$  along the punch, where they are compared with the reference solutions corresponding to  $n_{el} = 512$



and  $\beta_{exp} = 1$ . Analytical solutions deriving from Eqs. (66) are not reported in the figures because they are indistinguishable from the uniform mesh solutions. Analogous comparisons are presented in Fig. 6 for the case of a horizontal force  $P_x$  and in Fig. 7 for the case of a bending moment  $M$ . In all cases, the coarse graded mesh with  $n_{el} = 8$  and  $\beta_{exp} = 2$  proves to approximate the reference solutions very well.

## 4.2 Beam loaded by point force and moment

In this section, a beam with  $L/h = 10$  resting on an elastic substrate having  $c = 0.8$  is considered. Correspondingly,  $\nu_s = 0.20$  or  $\nu_s = 0.167$  for a generalised plane stress or plane strain state, respectively. In all examples presented, unless otherwise specified, a uniform mesh of  $n_{el} = 512$  beam elements is used, and the same discretization is applied to the substrate boundary. Moreover, the plotted values of horizontal and vertical displacements  $u_x$  and  $u_z$  refer to the substrate boundary. In some case, for comparison, horizontal displacements  $u_{bx,0}$  of the beam at  $z = 0$  are reported in the plots.

### 4.2.1 Beam loaded by a vertical point force $P_z$ at midspan

The case of a beam with  $\alpha L = 10$  perfectly bonded to an elastic half-plane and loaded by a vertical point force  $P_z$  at midspan is considered first. Dimensionless displacements and reactions along the substrate boundary are reported in Fig. 8 for both an Euler-Bernoulli beam ( $\phi = 0$ , thick solid line) and a Timoshenko beam ( $\phi = 0.3$ , thin solid line). In particular, the corresponding plots of horizontal displacements  $u_x$  (Fig. 8a) clearly indicate that the beam-substrate systems tend to stretch in the neighbourhood of the loaded cross-section, and to contract far away from it. When the horizontal displacements are evaluated along the beam axis, a completely different behaviour is observed. For example, for the Euler-Bernoulli beam a contraction of the whole beam axis is obtained, i.e.,  $u_{bx,0} > 0$  for  $x/L < 0$  and  $u_{bx,0} < 0$  for  $x/L > 0$  (dash-dot line in Fig. 8a). Therefore, for perfect adhesion,  $u_x$  turns out to be strongly influenced by the contribution of term  $\phi h/2$ . Moreover,

the significant discrepancy in the responses of Euler-Bernoulli and Timoshenko beams emphasizes the crucial role played by the shear deformations. This feature is even more evident from the plot of tangential reactions  $r_x$  (Fig. 8b), which is continuous for the shear-rigid beam, but shows a singularity at midspan for the shear-flexible beam. With regard to vertical displacements  $u_z$  (Fig. 8c), a wedge-shaped plot is obtained for the Timoshenko beam, showing a maximum deflection 56% larger than the Euler-Bernoulli beam. At the same section, the Timoshenko beam shows a singularity also in normal reactions  $r_z$  (Fig. 8d). This aspect was already noted in [26]. Furthermore, it is worth observing that, at the beam end sections, the normal reactions for the two beams take opposite sign.

For comparison, the results obtained for the Euler-Bernoulli beam ( $\phi = 0$ ) in frictionless contact with the substrate are also reported in Fig. 8 (dashed line). In particular, differently from the perfectly bonded beam, the frictionless condition yields contraction along the whole beam-substrate interface (Fig. 8a). Moreover, as expected,  $r_x = 0$  everywhere (Fig. 8b). With regard to vertical displacements  $u_z$  (Fig. 8c), for the beam in frictionless contact a maximum increase of 47% is obtained with respect to the perfect adhesion case. Finally, vertical reactions  $r_z$  (Fig. 8d) obtained for the Euler-Bernoulli beam do not seem to depend appreciably on the contact condition, with the exception of the cross-sections lying in the range  $|x/L| > 0.40$ .

The comparison between perfect adhesion and frictionless contact condition is re-proposed in Fig. 9 for a more flexible Euler-Bernoulli beam with  $\alpha L = 100$ . In this case, the two different contact conditions lead to substantially coincident results in terms of displacements  $u_x$  (Fig. 9a). With regard to tangential reactions  $r_x$  (Fig. 9b) for the beam in perfect adhesion, only the cross-sections lying in the range  $-0.18 \leq x/L \leq 0.18$  show  $r_x \neq 0$ , whereas, as is obvious, for the beam in frictionless contact  $r_x = 0$  everywhere. The beam responses in terms of  $u_z$  (Fig. 9c) and  $r_z$  (Fig. 9d) show larger values for the frictionless contact case only in proximity of the loaded cross-section. With regard to displacements  $u_x$ , an intermediate behaviour between those shown in Fig. 8a ( $\alpha L = 10$ ) and in Fig. 9a ( $\alpha L = 100$ ) is illustrated in Fig. 10a for  $\alpha L = 40$ . In particular, for the

perfectly bonded beam, a contraction at the beam-substrate interface is observed with the exception of a very narrow region centred on the loaded cross-section, where a stretching occurs (solid line in Fig. 10a). Note that, differently from what is observed in Fig. 8a, displacements  $u_{bx,0}$  at the centreline of the perfectly bonded beam (dash-dot line in Fig. 10a) are always larger than displacements  $u_x$  obtained for the beam in frictionless contact (dashed line in Fig. 10a).

The influence of the shear deformations on the normal reaction in proximity of the loaded cross-section is then analysed for different values of  $\alpha L$ . In particular, an Euler-Bernoulli beam ( $\phi = 0$ ) and a Timoshenko beam with  $\phi = 0.3$  are considered. An accurate description of the normal reactions is searched for using a uniform mesh of 1024 elements. Reported in Fig. 10b are reactions  $r_z(0)$  and  $r_z(L/1024)$  versus  $\alpha L$  for the Euler-Bernoulli and the Timoshenko beam, respectively. Note that for the shear-flexible beam, showing a singularity in the normal reaction at  $x = 0$  (Fig. 8d), one of the nodes closest to the beam centroid, located at  $x = L/1024$ , is chosen. The figure shows the numerical solutions for both perfect adhesion (thick solid lines) and frictionless contact (thick dashed lines). It can be noted that for  $\alpha L \leq 1$  the normal reactions for the two beams asymptotically tend to those of the rigid punch (thin solid and dashed lines). For larger values of  $\alpha L$ , the normal reaction for the Timoshenko beam is significantly larger than that for the Euler-Bernoulli beam.

#### 4.2.2 Comparison with other numerical formulations

With the purpose to evaluate the numerical performance of the present analysis, a beam perfectly bonded to an elastic half-plane is also analysed using two traditional numerical methods: a standard FE model that uses two-dimensional elastic elements to describe the soil and the approach proposed in [16, 17].

With regard to the two-dimensional FE model, the soil is modelled by means of quadrilateral elements in plane state. Three different square soil meshes are compared, showing total width equal to  $8L$  (Fig. 11a),  $16L$  (Fig. 11b) and  $32L$  (not shown graphically because of the very large dimensions), with  $L$  being the beam span length. In the following, these meshes are referred to as

FEM 8L, FEM 16L and FEM 32L, respectively. For all cases, at the boundaries, the displacements in the normal direction are fixed. Since for a relatively slender beam non-negligible horizontal displacements are to be expected for most of the beam length (see for example Figs. 9a for  $\alpha L = 100$  and Fig. 10a for  $\alpha L = 40$ ), FEM 16L and FEM 32L meshes were introduced with the aim to provide a more accurate description of the beam horizontal displacement. Two nested square meshes, showing widths equal to  $4L$  and  $2L$  for FEM 8L, to  $8L$  and  $4L$  for FEM 16L, and, finally, to  $16L$  and  $8L$  for FEM 32L, are built close to the foundation beam. Each edge of the quadrilateral elements of the smaller mesh has the same size of the beam elements. In Figs. 11, the case of the foundation beam subdivided into 4 beam FEs is shown for meshes FEM 8L and FEM 16L. The adopted meshes allow for the accurate solution to the soil-structure interaction problem with a number of FEs lower than that required by a simpler uniform mesh of quadrilateral elements.

With regard to the approach proposed in [17], a piecewise constant pressure having resultants applied to the nodes of the beam elements is adopted (Fig. 12). It is worth noting that a half of the end constant pressures lie outside the foundation beam. Inserting piecewise constant surface tractions into Eq. (8) yields the following expressions for the nodal displacements:

$$\mathbf{u}_x = \mathbf{G}_{C,xx} \mathbf{r}_x + c \mathbf{G}_{C,xz} \mathbf{r}_z \quad (68a)$$

$$\mathbf{u}_z = \mathbf{G}_{C,zz} \mathbf{r}_z + c \mathbf{G}_{C,zx} \mathbf{r}_x \quad (68b)$$

where

$$g_{C,xx,ij} = -\frac{1}{\pi E} \left[ [(x_j - x_i) + l_i/2] \ln \left( \frac{(x_j - x_i) + l_i/2}{l_i/2} \right)^2 - [(x_j - x_i) - l_i/2] \ln \left( \frac{(x_j - x_i) - l_i/2}{l_i/2} \right)^2 \right] \quad (69)$$

corresponds to the classical solution due to a uniform distribution of surface tractions [12] and

$$g_{C,xz,ij} = \frac{1}{E} \begin{cases} -l/2 & \text{if } i > j \\ 0 & \text{if } i = j \\ l/2 & \text{if } i < j \end{cases} \quad (70)$$

With arguments similar to those reported in Section 3.2, the relations  $\mathbf{G}_{C,zz} = \mathbf{G}_{C,xx}$  and  $\mathbf{G}_{C,xz} = \mathbf{G}_{C,xz}^T$  hold. Thus, the following matrix expression of Eqs. (68a, b) is obtained:

$$\begin{bmatrix} \mathbf{u}_x \\ \mathbf{u}_z \end{bmatrix} = \begin{bmatrix} \mathbf{G}_{C,xx} & c\mathbf{G}_{C,xz} \\ c\mathbf{G}_{C,xz}^T & \mathbf{G}_{C,zz} \end{bmatrix} \begin{bmatrix} \mathbf{r}_x \\ \mathbf{r}_z \end{bmatrix} = \mathbf{G}_C \mathbf{r} \quad (71)$$

Differently from Eq. (27), the nodal rotations do not appear in Eq. (71); thus, nodal rotations of the beam are independent of those resulting in the substrate boundary due to the surface tractions. Accordingly, the resulting soil matrix  $\mathbf{K}_{C,\text{soil}}$  coincides with  $\mathbf{G}_C^{-1}$  as far as nodal displacements are concerned and has rows and columns of zeros in correspondence of the nodal rotations. Finally, the soil-structure interaction problem can be solved by replacing  $\mathbf{K}_{\text{soil}}$  with  $\mathbf{K}_{C,\text{soil}}$  in Eq. (30b).

In the case of beams, indicating with  $n_{el}$  the number of beam FEs, the number of equations,  $n_{eq}$ , associated with the present analysis (PA) is given by  $n_{eq}^{(\text{PA})} = 5n_{el} + 3$ . Moreover, the number of equations associated with meshes FEM 8L, FEM 16L and FEM 32L is given by  $n_{eq}^{(8L)} = 20.1n_{el}^2$ ,  $n_{eq}^{(16L)} = 80.4n_{el}^2$  and  $n_{eq}^{(32L)} = 321.6n_{el}^2$ , respectively (note that, for meshes FEM 8L and FEM 16, the case for  $n_{el} = 4$  is depicted in Fig. 11). Finally, with regard to the approach proposed in [16, 17], a matrix inversion is required, which is computationally equivalent to the solution to  $2(n_{el} + 1)$  systems of  $2(n_{el} + 1)$  algebraic equations. Therefore, such an approach gives rise to a number of equations  $n_{eq}^{(\text{C})} = 3(n_{el} + 1) + 4(n_{el} + 1)^2$ . In the case of a rigid punch, the number of equations associated with the present analysis reduces to  $n_{eq}^{(\text{PA})} = 2n_{el} + 3$ .

Because no exact solution to the adhesive contact problem for flexible beams is available in the literature, the convergence properties of the proposed formulation are preliminarily compared with those exhibited by the other formulations for the case of a rigid flat punch. To this aim, the FE-BIE model reduces to the form presented in Section 3.6, whereas, in the FE models and in the approach proposed in [17], the (flexible) beam elements are replaced with (rigid) FEs characterised by a parameter  $\alpha L = 0.5$ . As already abovementioned (Section 4.1), an analytical solution to such a problem exists, and the proposed formulation is capable to recover this solution accurately (Fig. 4).

With the purpose of a convergence test, a rigid flat punch subjected to a bending moment  $M$  is considered. For each of the numerical models compared, a series of mesh refinements is obtained by letting  $n_{el}$  progressively take the values 8, 16, 32, 64, 128, 254, 512 and 1024. The analytical solution in terms of rotation, i.e., Eq. (64b), is used as reference solution for the test. The test results are reported in Fig. 13 in terms of relative error  $e_{M\varphi} = |M/\varphi_M - M/\varphi_o| / (M/\varphi_M)$  versus number of equations  $n_{eq}$ , with  $\varphi_o$  and  $\varphi_M$  indicating the rotations provided by the generic numerical formulation and by Eq. (64b), respectively. It can readily be observed that, in the log-log representation of Fig. 13, all models, though with different slopes, converge almost linearly to the exact solution, as is testified by the progressive reductions of error  $e_{M\varphi}$  with  $n_{eq}$ . However, the proposed FE-BIE model exhibits a convergence rate larger than twice those shown by the other models. In other words, at equal accuracy in the numerical solution, the proposed model is computationally more efficient. This feature justifies the use of the proposed model as the reference in the numerical examples presented below.

A further comparison of the various formulations is then carried out with reference to an Euler-Bernoulli beam with  $\alpha L = 20$  and  $L/h = 10$ , and subjected to a point force  $P_z$  at midspan or at one end section is chosen. For each of the numerical models compared, a series of mesh refinements is obtained by letting  $n_{el}$  take the same values as for the case of the rigid punch just investigated. The numerical solution obtained with the present analysis by discretizing the beam with 4096 equal FEs is used as reference solution for the comparison.

The test results are reported in Fig. 14 in terms of relative error  $e_M = |M_{\max} - M_{\text{ref}}| / |M_{\text{ref}}|$  versus the number of equations  $n_{eq}$ , where  $M_{\max}$  indicates the maximum bending moment in the beam obtained from the various models for a generic discretization, and  $M_{\text{ref}}$  represents the maximum bending moment corresponding to the reference solution. In particular, for  $P_z$  acting at midspan (Fig. 14a)  $M_{\text{ref}} = +0.02323 P_z L$  (sagging bending moment with tension in bottom fibres), whereas for  $P_z$  acting at the beam end section (Fig. 14b)  $M_{\text{ref}} = -0.01567 P_z L$  (hogging bending moment with tension in top fibres).

It can readily be observed from Fig. 14 that, at equal  $n_{eq}$ , the solution provided by the proposed model is significantly more accurate and presents higher convergence rate than the other formulations. However, it is to be recognised that the number of elements  $n_{el}$ , rather than the number of equations  $n_{eq}$ , is a more representative parameter to compare the convergence properties of the numerical models. Therefore, some further remarks are presented by assuming the same number of beam elements, though remembering that at equal  $n_{el}$  the computing time of the present formulation is noticeably lower than that required by the other numerical models. For example, for the beam with  $P_z$  acting at midspan (Fig. 14a), assuming  $n_{el} = 32$  yields  $e_M = 2.0\%$ ,  $2.3\%$  and  $1.3\%$  for the present analysis (PA), Cheung's solution [17] and all two-dimensional FE models, respectively. For the beam with  $P_z$  applied to one end beam section (Fig. 14b), a mesh refinement is required to obtain errors of the same order of magnitude as the previous case. Then, assuming  $n_{el} = 256$  yields  $e_M = 1.7\%$ ,  $4.6\%$  and  $3.0\%$  for the present analysis (PA), Cheung's solution [17] and mesh FEM 8L, respectively.

Table 1 reports constant  $C$  and exponent  $\lambda$  of convergence rate  $C n_{eq}^{-\lambda}$  for the curves shown in Figs. 14a, b (Euler-Bernoulli beam). The present analysis yields an exponent  $\lambda$  larger than 1.95 times the exponents provided by the other formulations. The parameters of the convergence rate for a Timoshenko beam with  $\phi = 0.3$  are also reported in Table 1. In particular, for  $P_z$  acting at midspan, the present analysis yields an exponent  $\lambda$  that is 1.93 times the other exponents. For the same Timoshenko beam, an error  $e_M = 1.8\%$  is obtained from the present analysis with  $n_{el} = 128$ . Because of the portions of the piecewise constant pressure lying beyond the beam end sections (Fig. 12), Cheung's solution [17] gives the same relative error as the present analysis with  $n_{el} = 256$ . The two-dimensional FE models provide  $e_M = 2.1\%$  with  $n_{el} = 128$ . Moreover, for a Timoshenko beam with  $P_z$  applied to one end section, the present analysis yields  $e_M = 2.1\%$  with  $n_{el} = 512$  and a value of the exponent  $\lambda$  that is 2.7 times larger than the other exponents (Table 1). To obtain the same numerical error with the other methods, more than 2,048 equal beam FEs are to be used.

In conclusion, the present model can be considered effective to solve beam-soil problems, and a number  $n_{el} = 512$  of equal beam FEs gives accurate solutions for all cases reported in the following.

#### 4.2.3 Beam loaded by a horizontal point force $P_x$ at midspan or at one end section

When a beam bonded to an elastic substrate is subjected to a horizontal force  $P_x$ , the solution to the beam-substrate interaction problem does not appreciably depend on parameter  $\phi$ , and the distinction between Euler-Bernoulli and Timoshenko theories becomes negligible. The comparison between a beam showing  $\alpha L = 10$  and a bar with equal cross-section but zero bending stiffness, corresponding to  $\beta L = 0.83$ , is reported in Fig. 15 for the horizontal force acting at midspan. In particular, neglecting the beam bending stiffness yields an overall reduction of horizontal displacements (Fig. 15a), that attains approximately 30% in correspondence of the centroidal cross-section. Nevertheless, with regard to horizontal reactions  $r_x$  (Fig. 15b), the influence of the bending stiffness proves not to be particularly significant. This is also true for  $u_z$  (Fig. 15c), with the exception of the two beam regions  $|x/L| > 0.30$ , where differences in the vertical displacements up to approximately 20% are observed at the beam end sections. The normal reactions (Fig. 15d) for the beam show a discontinuity at  $x = 0$ , whereas for zero bending stiffness,  $r_z$  is equal to zero everywhere. Analogous considerations hold when the horizontal force is assumed to act at one end section (Fig. 16), with the exception that the horizontal displacements of the bar are larger than those of the beam for  $x/L > 0.4$  (Fig. 16a).

#### 4.2.4 Beam loaded by a bending moment $M$ at midspan

The case of an Euler-Bernoulli beam ( $\phi = 0$ ) and a Timoshenko beam with  $\phi = 0.3$ , both showing  $\alpha L = 10$  and perfectly bonded to an elastic half-plane, is investigated (Fig. 17). Horizontal displacements  $u_x$  (Fig. 17a) for the shear-flexible beam (thin solid line) noticeably exceed those for the shear-rigid beam (thick solid line). In particular, at  $x = 0$  the value of  $u_x$  attained from the Timoshenko beam is approximately 60% larger than that computed for the Euler-Bernoulli beam.



The dash-dot line in Fig. 17a refers to the horizontal displacements at the centreline of the perfectly bonded Euler-Bernoulli beam. In particular, for  $-0.18 \leq x/L \leq 0.18$ ,  $u_{bx,0}$  takes significantly lower absolute values, and even opposite sign, with respect to displacements  $u_x$  evaluated at the substrate boundary. Hence, the strong relevance of term  $\varphi h/2$  is confirmed. Although the shear deformations have significant influence on displacements  $u_x$ , tangential reactions  $r_x$  for the Timoshenko beam coincide almost everywhere with those computed for the Euler-Bernoulli beam (Fig. 17b). Moreover, differently from the case of vertical load  $P_z$  (Fig. 8c, d), normal displacements (Fig. 17c) and reactions (Fig. 17d) for the Timoshenko beam are lower than the corresponding quantities for the Euler-Bernoulli beam for all cross-sections located in the range  $-0.4 \leq x/L \leq 0.4$ . Only in proximity of the beam end sections, i.e., for  $|x/L| > 0.4$ , the shear deformations lead to higher displacements and reactions along the  $x$ -axis.

For comparison, the results obtained for an Euler-Bernoulli beam with  $\alpha L = 10$  in frictionless contact with the substrate are also presented in Fig. 17 (dashed line). A completely different behaviour in terms of horizontal displacements is observed with respect to the Euler-Bernoulli beam in perfect adhesion. In particular, displacements  $u_x$  for the two contact conditions take opposite sign in a large interval of  $x/L$  values (Fig. 17a). The responses of the shear-rigid beam in terms of normal displacements (Fig. 17c) and reactions (Fig. 17d) for the two contact conditions are qualitatively similar, even if perfect adhesion leads to lower absolute values of  $u_z$  along the whole interface and larger absolute values of  $r_z$  for  $-0.14 \leq x/L \leq 0.14$ .

The horizontal displacements at the substrate boundary for an Euler-Bernoulli beam with  $\alpha L = 40$  are reported in Fig. 18a for both perfect adhesion (solid line) and frictionless contact (dashed line). Reported in the same figure is the plot of displacements  $u_{bx,0}$  evaluated along the centreline of the beam in perfect adhesion (dash-dot line). The example confirms that the contact condition has a noteworthy influence on the horizontal displacements. Moreover, near the midspan of the beam in perfect adhesion, displacements  $u_{bx,0}$  take not only opposite sign with respect to

displacements  $u_x$ , but also larger absolute values. Then, the role played by the beam cross-section rotation, already highlighted for  $\alpha L = 10$  in Fig. 17a, becomes crucial for more flexible beams.

The tangential reaction at midspan for an Euler-Bernoulli and a Timoshenko beam bonded to an elastic substrate is plotted in Fig. 18b versus  $\alpha L$ . These results follow from numerical models based on a uniform mesh of 1024 FEs. Note that, in this case, the shear deformations do not influence the beam response (an analogous consideration can also be made by observing in Fig. 17b the curves for the perfectly bonded Euler-Bernoulli and Timoshenko beams in proximity of  $x/L = 0$ ). The behaviour of a rigid punch is substantially re-obtained for  $\alpha L \leq 1$ .

### 4.3 Plane strain analysis of a two-bay frame resting on an isotropic elastic substrate

The present example is aimed at assessing the soil-structure interaction for the realistic case of a double-cell box culvert or tunnel (Fig. 19a), that is a very common structural typology usually made of reinforced concrete. The foundation structures and the upper slab with net span length 6.00 m, both showing thickness  $h = 1.20$  m, as well as the three 1m-thick abutments, are cast-in-place members. Across the largest span, left and intermediate abutments support 1.5m-high precast I-beams with 2m spacing, mutually connected at the top through a 0.2m-thick continuous slab. The resulting ribbed slab has a self-weight of 15 (kN/m)/m and second moment of area  $I = 0.34$  m<sup>4</sup>/m. To obtain monolithic connections between precast beams and abutments, suitable cast-in-place joints are provided at the beam supports. Then, the generic cross-section of the double-cell tunnel is reduced to the plane frame shown in Fig. 19b, having a uniform out-of-plane dimension  $b = 1$  m and span lengths  $L1 = 14.50$  m and  $L2 = 7.00$  m. Foundation R1 is modelled as a 1.2m-high rigid punch bonded to an isotropic, elastic half-plane, and discretized using a graded mesh with  $n_{el} = 8$  and  $\beta_{exp} = 2$ . Because of the larger flexibility in comparison with R1, foundation F2 is modelled using a uniform mesh of  $n_{el} = 20$  Euler-Bernoulli beam FEs in perfect adhesion with the substrate. According with Fig. 3 and the transformation rule reported in Section 3.5, column B1 is connected at the base to the top node of punch R1, resulting in a column height  $H1 = 7.20$  m. Conversely,

according with the formulation presented in Section 3.3, the FE-BIE elements used for foundation beam F2 have the centreline placed at a distance  $h/2 = 0.6$  m from the substrate boundary, leading columns B4 and B5 to have a total height  $H2 = 7.80$  m. For both the rigid punch and the foundation beam, one single soil element is used for each FE. Euler-Bernoulli beam FEs are used for members B1 to B5. A series of preliminary tests confirmed that the numerical model described ensures convergent solutions. A plane strain analysis is conducted by assuming  $E_s = 30$  MPa and  $\nu_s = 0.3$  for the substrate and  $E_b / (1 - \nu_b^2) = 30$  GPa for all structural elements. In particular, the two load cases shown in Fig. 19c are considered, i.e., the self-weight and a horizontal load  $p_x$  uniformly distributed along beams B2 and B3. This load can be viewed as a hypothetical seismic action of magnitude approximately equal to 20% of the structural self-weight.

Reported in Fig. 20a are the deformed shapes of the frame corresponding to the self-weight (solid line) and to the lateral load (dashed line) separately acting from one another. In the same figure, the undeformed shape is reported for comparison (dash-dot line). The maximum vertical deflection is observed in correspondence of the right-hand section of foundation beam F2 and is approximately 11 mm for both load cases. The frame lateral deflection due to the horizontal force is about 7 mm.

Tangential and normal reactions underneath foundations R1 and F2 are reported in Fig. 20b and Fig. 20c, respectively, for the two load cases. The maximum reactions are obtained for the frame subjected to self-weight. With the exception of the end elements of rigid punch R1, where the reactions tend to become excessive because of the foundation stiffness, the values of  $r_x$  and  $r_z$  obtained for foundations R1 and F2 for the frame subjected to self-weight are substantially comparable. On the other hand, in the presence of the lateral load, the responses of the two foundations in terms of tangential reactions  $r_x$  appear to be completely different (dashed lines in Fig. 20c).

Finally, ratio  $r_x/r_z$  obtained when vertical and lateral loads are applied simultaneously is reported in Fig. 20d. It can be noted that, with the exception of the end elements of the two foundations, ratio  $r_x/r_z$  linearly varies for both R1 and F2, taking values not larger than 0.3.

## 5 CONCLUSIONS

A coupled FE-BIE model for the analysis of prismatic beams and frames in perfect adhesion to a homogeneous, linearly elastic and isotropic two-dimensional half-space is proposed. In particular, the classical displacement based FE method is used to describe the response of beams or frames, whereas a BIE approach is used for the substrate boundary, where surface displacements are linked to the applied loads by means of a suitable Green's function. Under the assumption of plane strain or plane stress state, the variational formulation is obtained through the theorem of work and energy for exterior domains, with the independent unknown functions being represented by beam displacements and surface tractions. In the more general case, Timoshenko beam theory is used to account for the effects of the shear deformations. Locking-free cubic and quadratic Hermitian shape functions are selected to interpolate transverse deflection and rotation, respectively, whereas axial displacement is approximated by linear functions. In addition, piecewise constant shape functions are used to describe both tangential and normal surface tractions. If the beam strain energy is ignored, the beam behaves like a rigid punch resting on a two-dimensional half-space. When tangential tractions and external horizontal forces are set equal to zero, the proposed formulation may be applied to the analysis of frictionless contact problems. Finally, by neglecting the beam bending stiffness, the problem of a thin coating bonded to a half-plane is recovered.

A number of numerical examples are presented to show the effectiveness of the proposed formulation in the analysis of the soil-structure interaction. In the case of a rigid punch subjected to point forces or moments, the analytical solutions available in the literature in terms of punch rotation and soil reactions are re-obtained. Moreover, it is shown that good approximations of these solutions are ensured by a coarse, graded mesh of only 8 FEs.

In the case of a beam subjected to a vertical point force or a bending moment at midspan, the shear deformations have a significant influence on both tangential and normal surface displacements and soil reactions. Moreover, the difference between horizontal displacements evaluated along the substrate boundary and the beam axis indicates a noteworthy contribution of the beam section rotation. In addition, the perfect adhesion is shown to dramatically modify the beam response with respect to the condition of frictionless contact. Both for Euler-Bernoulli and Timoshenko beams subjected to vertical point loads, the numerical performance of the proposed model has shown an excellent convergence rate in comparison with those of other standard numerical methods. Finally, if the beam is subjected to a horizontal point force, the horizontal displacements are completely different from those obtained for a thin coating of equal cross-section, indicating a significant effect of the beam bending stiffness.

The last example concerns the soil-structure interaction analysis for a double-cell box tunnel. Assuming a state of plane strain, the tunnel cross-section is identified with a two-bay frame subjected to self-weight and a uniformly distributed lateral load. The loads are transferred to the soil by means of a rigid punch and a foundation beam in perfect adhesion with the substrate boundary. Rigid punch and foundation beam are discretized by means of a graded mesh of 8 FEs and a uniform mesh of 20 FEs, respectively. The proposed formulation is shown to be effective in the evaluation of frame deflections and soil reactions.

## **ACKNOWLEDGMENTS**

The present investigation was developed in the framework of the Research Program FAR 2013 of the University of Ferrara. Moreover, the analyses were developed within the activities of the (Italian) University Network of Seismic Engineering Laboratories–ReLUIS in the research program funded by the (Italian) National Civil Protection – Progetto Esecutivo 2015 – Research Line “Reinforced Concrete Structures”, WP2.

## REFERENCES

- [1] Helgeson DE, Aydin A. Characteristics of joint propagation across layer interfaces in sedimentary rocks. *J Struct Geol* 1991; 13(8):897–911.
- [2] Voevodin AA, Zabinski JS. Nanocomposite and nanostructured tribological materials for space applications. *Compos Sci Technol* 2005; 65(5):741–748.
- [3] Oehlers DJ. Reinforced concrete beam with plates glued to their soffits. *J Struct Eng* 1992; 118(8):2023–2038.
- [4] Akbar I, Oehlers DJ, Mohamed Ali MS. Derivation of the bond-slip characteristics for FRP plated steel members. *J Constr Steel Res* 2010; 66(8-9):1047–1056.
- [5] Varastehpour H, Hamelin P. Strengthening of concrete beams using fiber-reinforced plastics. *Mater Struct* 1997; 30(197):160–166.
- [6] Tsai MY, Morton J. The effect of a spew fillet on adhesive stress distribution in laminated composite single-lap joints. *Compos Struct* 1995, 32(1-4):123–131.
- [7] Belingardi G, Goglio L, Tarditi A. Investigating the effect of spew and chamfer size on the stresses in metal/plastics adhesive joints. *Int J Adhes Adhes* 2002, 22(4):273–282.
- [8] Da Silva LFM, Adams RD. Techniques to reduce the peel stresses in adhesive joints with composites. *Int J Adhes Adhes* 2007, 27(3):227–235.
- [9] Shen YL. *Constrained Deformation of Materials, Devices, Heterogeneous Structures and Thermo-Mechanical Modeling*. New York: Springer; 2010.
- [10] Selvadurai APS. *Elastic analysis of soil-foundation interaction. Developments in Geotechnical Engineering*, Elsevier Science; 1979.
- [11] Wang YH, Tham LG, Cheung YK. Beams and plates on elastic foundations: a review. *Prog Struct Eng Mater* 2005; 7(4):174–182.
- [12] Johnson KL. *Contact mechanics*. Cambridge: Cambridge University Press; 1985.
- [13] Kachanov ML, Shafiro B, Tsukrov I. *Handbook of elasticity solutions*. Dordrecht: Kluwer Academic Publishers; 2003.

- [14] Biot MA. Bending of an infinite beam on an elastic foundation. *J Appl Mech* 1937; 4:A1–A7.
- [15] Felippa CA. A study of optimal membrane triangles with drilling freedoms. *Comput Meth Appl Mech Eng* 2003; 192(16-18):2125–2168.
- [16] Cheung YK, Zienkiewicz OC. Plates and tanks on elastic foundations - an application of finite element method. *Int J Solids Structure* 1965; 1(4):451–461.
- [17] Cheung YK, Nag DK. Plates and beams on elastic foundation - linear and non-linear behaviour. *Geotechnique* 1968; 18(2):250–260.
- [18] Wang SK, Sargious M, Cheung YK. Advanced analysis of rigid pavements. *J Transp Eng-ASCE* 1972; 98(1):37–44.
- [19] Kikuchi N, Oden J. Contact problems in elasticity. A study of variational inequalities and finite element methods. Philadelphia: SIAM; 1988.
- [20] Kikuchi N. Beam bending problems on a Pasternak foundation using reciprocal variational-inequalities. *Q Appl Math* 1980; 38(1):91–108.
- [21] Bielak J, Stephan E. A modified Galerkin procedure for bending of beams on elastic foundations. *SIAM J Sci Stat Comput* 1983; 4(2):340–352.
- [22] Guarracino F, Minutolo V, Nunziante L. A simple analysis of soil-structure interaction by BEM-FEM coupling. *Eng Anal Bound Elem* 1992; 10(4):283–289.
- [23] Bode C, Hirschauer R, Savidis SA. Soil-structure interaction in the time domain using half-space Green's functions. *Soil Dyn Earthq Eng* 2002; 22(4):283–295.
- [24] Ribeiro DB, Paiva JB. An alternative BE–FE formulation for a raft resting on a finite soil layer. *Eng Anal Bound Elem* 2015; 50:352–359.
- [25] Aleynikov S. Spatial Contact Problems in Geotechnics. *Boundary-Element Method*. Berlin Heidelberg: Springer-Verlag; 2011.
- [26] Tullini N, Tralli A. Static analysis of Timoshenko beam resting on elastic half-plane based on the coupling of locking-free finite elements and boundary integral. *Comput Mech* 2010; 45(2–3):211–225.

- [27] Tullini N, Tralli A, Lanzoni L. Interfacial shear stress analysis of bar and thin film bonded to 2D elastic substrate using a coupled FE-BIE method. *Finite Elem Anal Des* 2012; 55:42–51.
- [28] Tullini N, Tralli A, Baraldi D. Stability of slender beams and frames resting on 2D elastic half-space. *Arch Appl Mech* 2013; 83(3):467–482.
- [29] Tullini N, Tralli A, Baraldi D. Buckling of Timoshenko beams in frictionless contact with an elastic half-plane. *J Eng Mech* 2013; 139(7):824–831.
- [30] Cowper GR. The shear coefficient in Timoshenko's beam theory. *J Appl Mech ASME* 1966; 33:335–340.
- [31] Tullini N, Savoia M. Elasticity interior solution for orthotropic strips and the accuracy of beam theories. *J Appl Mech ASME* 1999; 66(2):368–373.
- [32] Gurtin ME, Sternberg E. Theorems in linear elastostatics for exterior domains. *Arch Ration Mech Anal* 1961; 8:99–119.
- [33] Reddy JN. On locking-free shear deformable beam finite elements. *Comput Meth Appl Mech Eng* 1997; 149(1-4):113–132.
- [34] Narayanaswami R, Adelman HM. Inclusion of transverse shear deformation in finite element displacement formulations. *AIAA J* 1974; 12(11):1613–1614.
- [35] Friedman Z, Kosmatka JB. An improved two-node Timoshenko beam finite element. *Comput Struct* 1993; 47(3):473–481.
- [36] Minghini F, Tullini N, Laudiero F. Locking-free finite elements for shear deformable orthotropic thin-walled beams. *Int J Numer Methods Eng* 2007; 72(7):808–834.
- [37] Vesic AB. Bending of beams on isotropic elastic medium. *J Eng Mech Div ASCE* 1961; 87(EM2):35–53.
- [38] Grigolyuk EI, Tolkachev VM. Contact problems in the theory of plates and shells, Moscow: Mir Publishers; 1987.
- [39] Hsiao GC, Wendland WL. A finite element method for some integral equations of the first kind. *J Math Anal Appl* 1977; 58(3):449–481.



- [40] Costabel M. Boundary integral operators on Lipschitz domains: Elementary results. *SIAM J Math Anal* 1988; 19(3):613–626.
- [41] Graham IG, McLean W. Anisotropic mesh refinement: the conditioning of Galerkin Boundary element matrices and simple preconditioners. *SIAM J Numer Anal* 2006, 44(4):1487–1513.

## Figure Captions

Fig. 1. Beam bonded to a two-dimensional half-space **(a)**, and free-body diagram **(b)**.

Fig. 2. Green's function  $g(x, \hat{x})$  related to point forces  $P_x(\hat{x})$ ,  $P_z(\hat{x})$  applied to the half-plane boundary

Fig. 3. Rigid footing placed on the half-plane boundary and connected to a beam-column.

Fig. 4. Rigid punch subjected to a horizontal force  $P_x$  or a bending moment  $M$ . Relative errors  $e_{P\phi} = |P_x/\phi_P - P_x/\phi_o|/(P_x/\phi_P)$  **(a)** and  $e_{M\phi} = |M/\phi_M - M/\phi_o|/(M/\phi_M)$  **(b)** versus  $n_{el}$  for uniform ( $\beta_{exp} = 1$ ) and graded mesh ( $\beta_{exp} = 2, 3$ ).  $\phi_P$  and  $\phi_M$  are the closed-form rotations (64a) and (64b), and  $\phi_o$  is the rotation obtained from the proposed formulation.

Fig. 5. Rigid punch loaded by a vertical point force  $P_z$  at midspan. Nondimensional tangential **(a)** and normal **(b)** reactions versus  $x/L$  obtained using a uniform mesh with  $n_{el} = 512$  (thick solid line) and a graded mesh with  $n_{el} = 8$ ,  $\beta_{exp} = 2$  (thin solid line with symbol).

Fig. 6. Rigid punch loaded by a horizontal point force  $P_x$  at midspan. Nondimensional tangential **(a)** and normal **(b)** reactions versus  $x/L$  obtained using a uniform mesh with  $n_{el} = 512$  (thick solid line) and a graded mesh with  $n_{el} = 8$ ,  $\beta_{exp} = 2$  (thin solid line with symbol).

Fig. 7. Rigid punch loaded by a bending moment  $M$  at midspan. Nondimensional tangential **(a)** and normal **(b)** reactions versus  $x/L$  obtained using a uniform mesh with  $n_{el} = 512$  (thick solid line) and a graded mesh with  $n_{el} = 8$ ,  $\beta_{exp} = 2$  (thin solid line with symbol).

Fig. 8. Beam ( $L/h=10$ ,  $\alpha L=10$ ) loaded by a vertical point force  $P_z$  at midspan. Nondimensional values of  $u_x$  **(a)**,  $r_x$  **(b)**,  $u_z$  **(c)**, and  $r_z$  **(d)** versus  $x/L$  for perfect adhesion with  $\phi = 0.0$  and  $0.3$  (thick and thin solid line), and for frictionless contact with  $\phi = 0.0$  (dashed line). Horizontal displacement  $u_{bx,0}$  (dash-dot line in **a**) is referred to the centreline of the beam in perfect adhesion with  $\phi = 0.0$ .

Fig. 9. Euler-Bernoulli beam ( $L/h=10$ ,  $\alpha L=100$ ,  $\phi = 0.0$ ) loaded by a vertical point force  $P_z$  at midspan. Nondimensional values of  $u_x$  **(a)**,  $r_x$  **(b)**,  $u_z$  **(c)**, and  $r_z$  **(d)** versus  $x/L$  for perfect adhesion (solid line) and frictionless contact (dashed line).

Fig. 10. Beam ( $L/h=10$ ) loaded by a vertical point force  $P_z$  at midspan, comparison between perfect adhesion (solid line) and frictionless contact (dashed line). Nondimensional values of  $u_x$  versus  $x/L$  obtained for  $\alpha L=40$  and  $\phi = 0.0$  (a); and nondimensional values of  $r_z$  at or in proximity of midspan versus  $\alpha L$  obtained for  $\phi = 0.0$  and  $0.3$  (b). Horizontal displacement  $u_{bx,0}$  (dash-dot line in a) is referred to the beam centreline.

Fig. 11. Meshes adopted for the two-dimensional FE models with a foundation beam subdivided into 4 equal FEs. Models with mesh dimension  $8L$  (FEM 8L) (a) and  $16L$  (FEM 16L) (b).

Fig 12. Piecewise constant pressure elements adopted in [17].

Fig. 13. Rigid punch subjected to a bending moment  $M$ . Relative errors  $e_{M\phi} = |M/\phi_M - M/\phi_o|/(M/\phi_M)$  versus number of equation  $n_{eq}$ , with  $\phi$  representing the rotation obtained from the generic numerical model, and  $\phi_M$  being the closed-form rotation provided by Eq. (64b).

Fig. 14. Euler-Bernoulli beam ( $L/h=10$ ,  $\alpha L=20$ ) subjected to a vertical force  $P_z$  at midspan (a) and at one end section (b). Relative errors  $e_M = |M_{\max} - M_{\text{ref}}|/|M_{\text{ref}}|$  in terms of the maximum bending moment versus number of equation  $n_{eq}$  for the present analysis (PA), Cheung's solution [17] and meshes FEM 8L, FEM16L and FEM32L.

Fig. 15. Beam with  $L/h = 10$ ,  $\alpha L = 10$  (solid line) and thin coating with  $\beta L = 0.83$  (dashed line) in perfect adhesion to a half-plane, loaded by a horizontal point force  $P_x$  at midspan. Nondimensional values of  $u_x$  (a),  $r_x$  (b),  $u_z$  (c), and  $r_z$  (d) versus  $x/L$ .

Fig. 16. Beam with  $L/h = 10$ ,  $\alpha L = 10$  (solid line) and thin coating with  $\beta L = 0.83$  (dashed line) in perfect adhesion to a half-plane, loaded by a horizontal point force  $P_x$  at one end section. Nondimensional values of  $u_x$  (a),  $r_x$  (b),  $u_z$  (c), and  $r_z$  (d) versus  $x/L$ .

Fig. 17. Beam ( $L/h=10$ ,  $\alpha L=10$ ) loaded by a bending moment  $M$  at midspan. Nondimensional values of  $u_x$  (a),  $r_x$  (b),  $u_z$  (c), and  $r_z$  (d) versus  $x/L$  for perfect adhesion with  $\phi = 0.0$  and  $0.3$  (thick and thin solid line), and for frictionless contact with  $\phi = 0.0$  (dashed line). Horizontal displacement  $u_{bx,0}$  (dash-dot line in (a)) is referred to the centreline of the perfectly bonded beam with  $\phi = 0.0$ .

Fig. 18. Beam ( $L/h=10$ ) loaded by a bending moment  $M$  at midspan, comparison between perfect adhesion (solid line) and frictionless contact (dashed line). Nondimensional values of  $u_x$  versus  $x/L$  obtained for  $\alpha L=40$  and  $\phi = 0.0$  (**a**); and nondimensional values of  $r_x$  at midspan versus  $\alpha L$  obtained for  $\phi = 0.0$  and  $0.3$  (**b**). Horizontal displacement  $u_{bx,0}$  (dash-dot line in (**a**)) is referred to the beam centreline.

Fig. 19. Cross-section geometry of the double-cell tunnel investigated (**a**); corresponding two-bay frame analysed under plane strain assumption (**b**); and load cases considered (**c**, **d**).

Fig. 20. Frame deflections (**a**) and reactions underneath rigid punch and foundation beam (**b**, **c**) for the structure subjected to self-weight (solid line) and lateral load (dashed line). Ratio  $r_x/r_z$  for the two load cases acting simultaneously (**d**). Dash-dot line in (**a**) represents the undeformed frame.

### Table Caption

Table 1. Euler-Bernoulli and Timoshenko ( $\phi = 0.3$ ) beams ( $L/h=10$ ,  $\alpha L=20$ ) subjected to a vertical force  $P_z$  at midspan and at one end section. Parameters of the convergence rate expression  $C n_{eq}^{-\lambda}$  for relative error  $e_M$  in terms of the maximum bending moment. Comparison between present analysis (PA), Cheung's solution [17] and two-dimensional FE models.

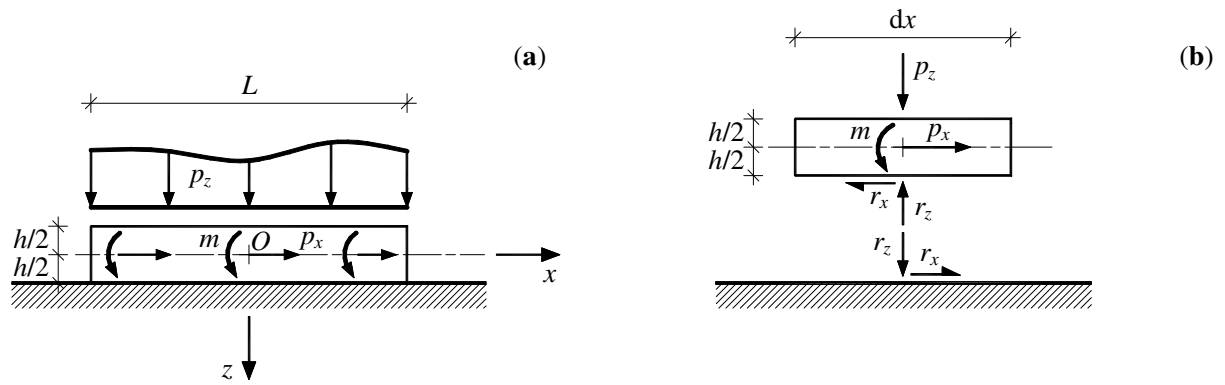


Fig. 1. Beam bonded to a two-dimensional half-space (a), and free-body diagram (b).

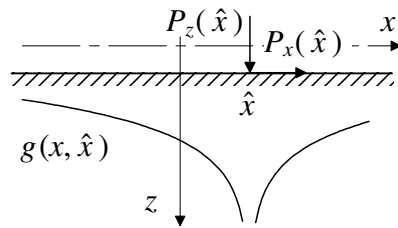


Fig. 2. Green's function  $g(x, \hat{x})$  related to point forces  $P_x(\hat{x})$ ,  $P_z(\hat{x})$  applied to the half-plane boundary

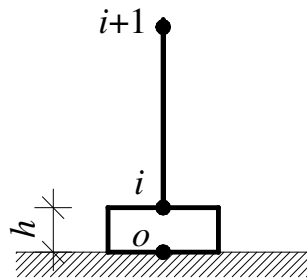


Fig. 3. Rigid footing placed on the half-plane boundary and connected to a beam-column.

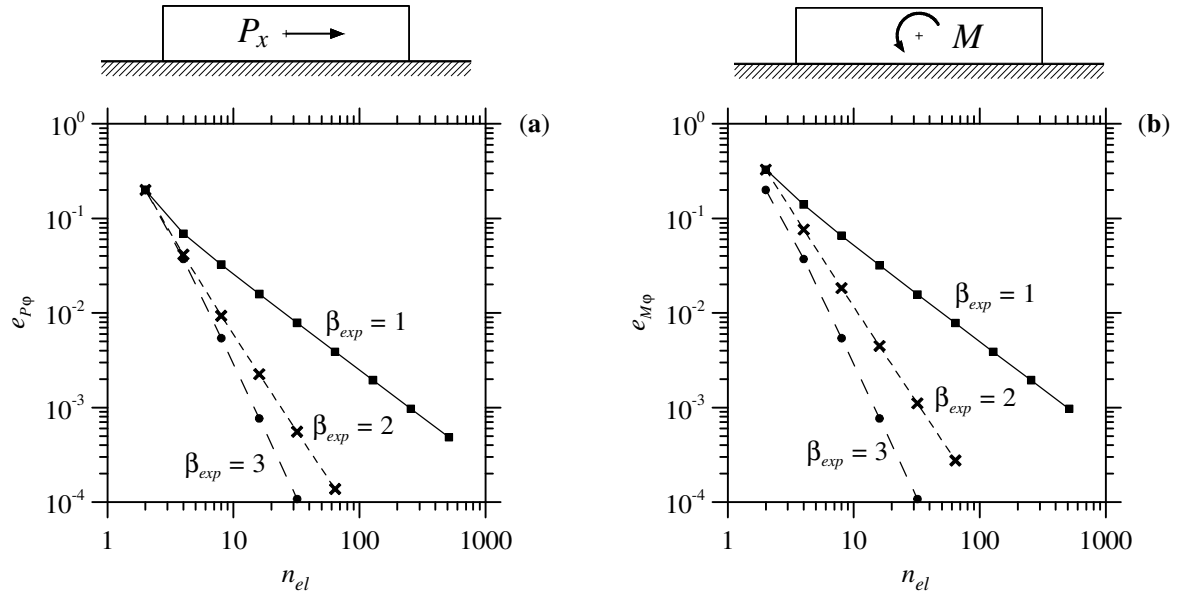


Fig. 4. Rigid punch subjected to a horizontal force  $P_x$  or a bending moment  $M$ . Relative errors  $e_{P\phi} = |P_x/\phi_P - P_x/\phi_o|/(P_x/\phi_P)$  (a) and  $e_{M\phi} = |M/\phi_M - M/\phi_o|/(M/\phi_M)$  (b) versus  $n_{el}$  for uniform ( $\beta_{exp} = 1$ ) and graded mesh ( $\beta_{exp} = 2, 3$ ).  $\phi_P$  and  $\phi_M$  are the closed-form rotations (64a) and (64b), and  $\phi_o$  is the rotation obtained from the proposed formulation.

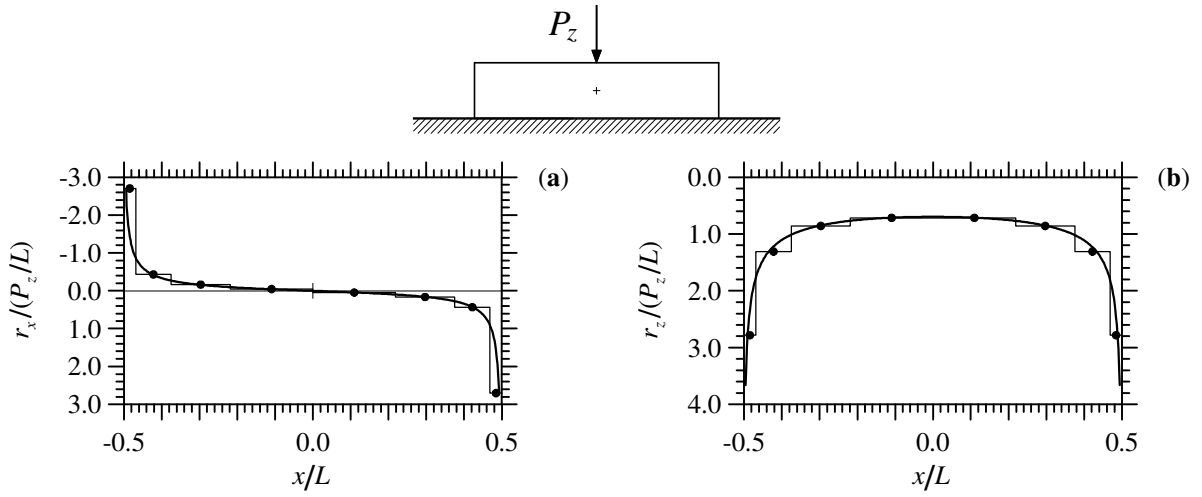


Fig. 5. Rigid punch loaded by a vertical point force  $P_z$  at midspan. Nondimensional tangential (a) and normal (b) reactions versus  $x/L$  obtained using a uniform mesh with  $n_{el} = 512$  (thick solid line) and a graded mesh with  $n_{el} = 8$ ,  $\beta_{exp} = 2$  (thin solid line with symbol).

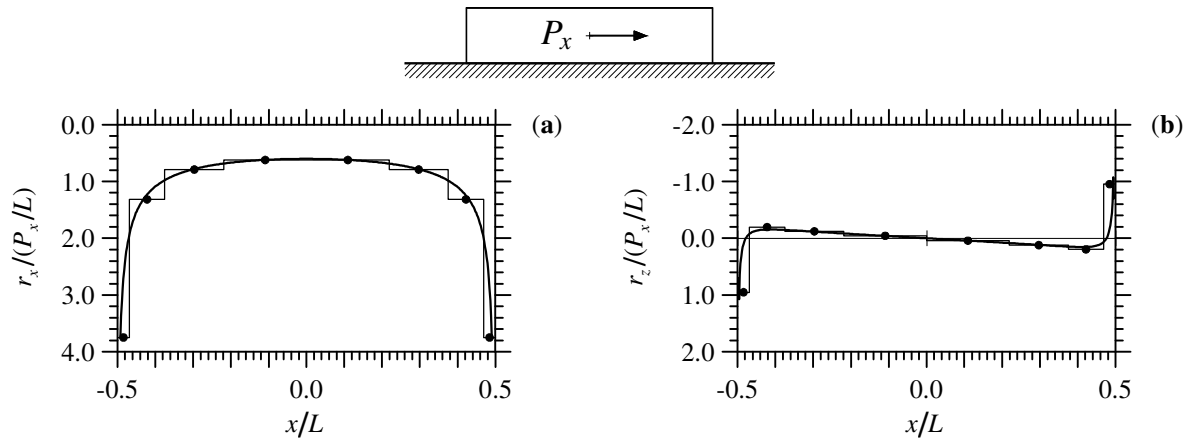


Fig. 6. Rigid punch loaded by a horizontal point force  $P_x$  at midspan. Nondimensional tangential (a) and normal (b) reactions versus  $x/L$  obtained using a uniform mesh with  $n_{el} = 512$  (thick solid line) and a graded mesh with  $n_{el} = 8$ ,  $\beta_{exp} = 2$  (thin solid line with symbol).



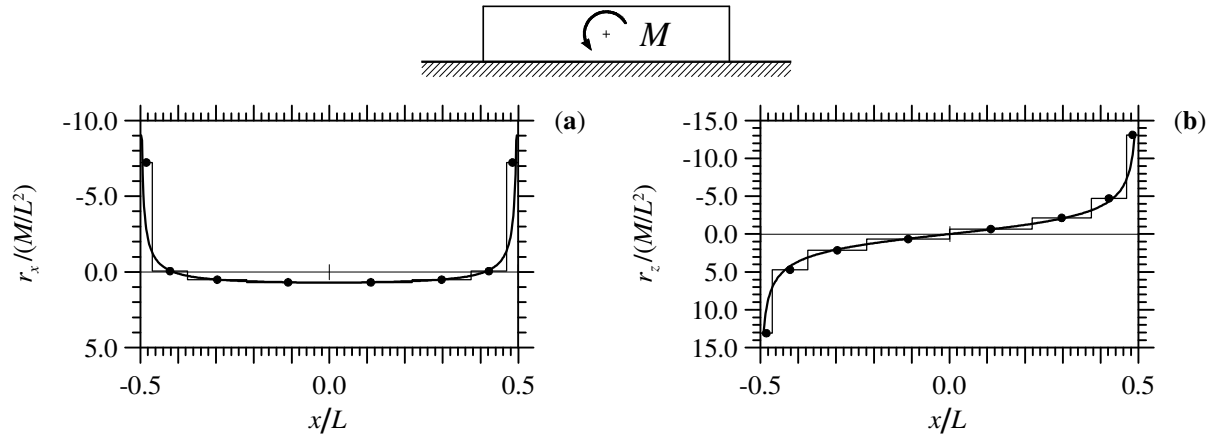


Fig. 7. Rigid punch loaded by a bending moment  $M$  at midspan. Nondimensional tangential (a) and normal (b) reactions versus  $x/L$  obtained using a uniform mesh with  $n_{el} = 512$  (thick solid line) and a graded mesh with  $n_{el} = 8$ ,  $\beta_{exp} = 2$  (thin solid line with symbol).

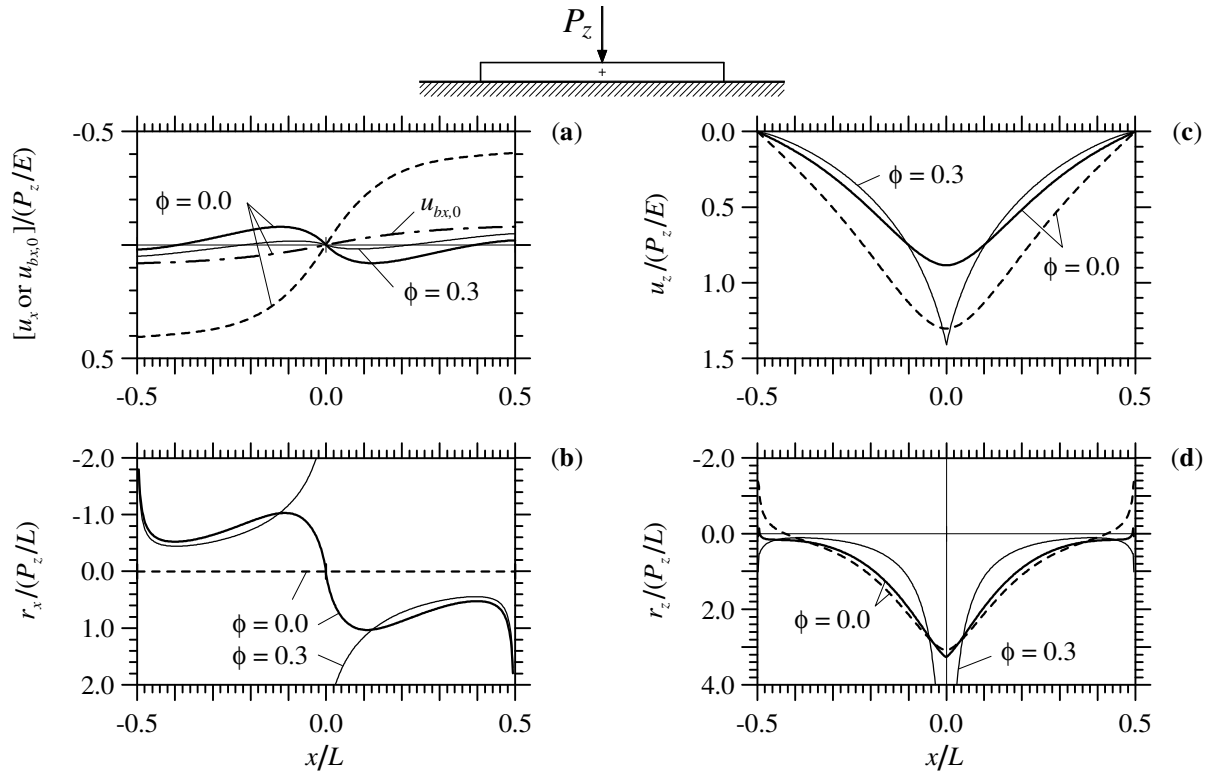


Fig. 8. Beam ( $L/h=10$ ,  $\alpha L=10$ ) loaded by a vertical point force  $P_z$  at midspan. Nondimensional values of  $u_x$  (a),  $r_x$  (b),  $u_z$  (c), and  $r_z$  (d) versus  $x/L$  for perfect adhesion with  $\phi = 0.0$  and  $0.3$  (thick and thin solid line), and for frictionless contact with  $\phi = 0.0$  (dashed line). Horizontal displacement  $u_{bx,0}$  (dash-dot line in a) is referred to the centreline of the beam in perfect adhesion with  $\phi = 0.0$ .

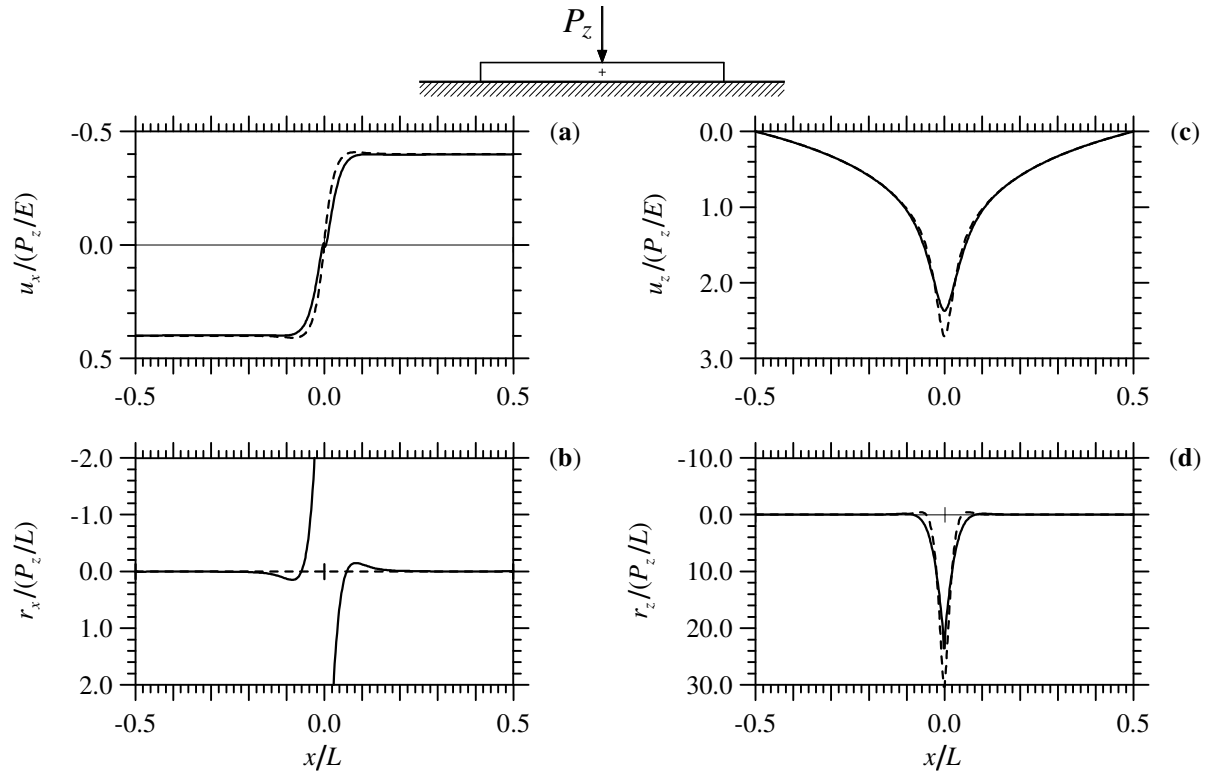


Fig. 9. Euler-Bernoulli beam ( $L/h=10$ ,  $\alpha L=100$ ,  $\phi = 0.0$ ) loaded by a vertical point force  $P_z$  at midspan. Nondimensional values of  $u_x$  (a),  $r_x$  (b),  $u_z$  (c), and  $r_z$  (d) versus  $x/L$  for perfect adhesion (solid line) and frictionless contact (dashed line).

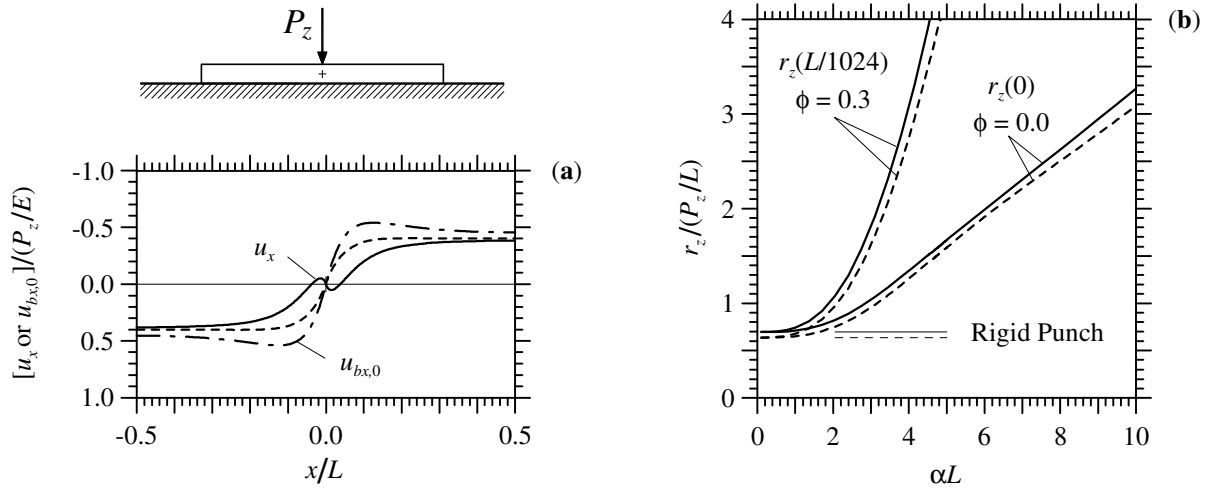
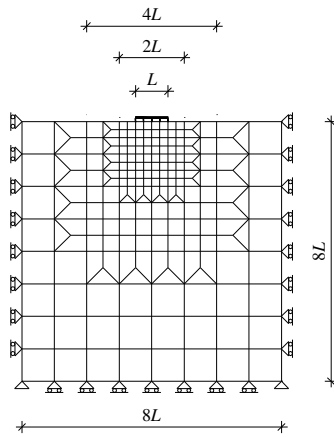


Fig. 10. Beam ( $L/h=10$ ) loaded by a vertical point force  $P_z$  at midspan, comparison between perfect adhesion (thick solid line) and frictionless contact (dashed line). Nondimensional values of  $u_x$  versus  $x/L$  obtained for  $\alpha L=40$  and  $\phi = 0.0$  (a); and nondimensional values of  $r_z$  at or in proximity of midspan versus  $\alpha L$  obtained for  $\phi = 0.0$  and  $0.3$  (b). Horizontal displacement  $u_{bx,0}$  (dash-dot line in a) is referred to the beam centreline.

(a)



(b)

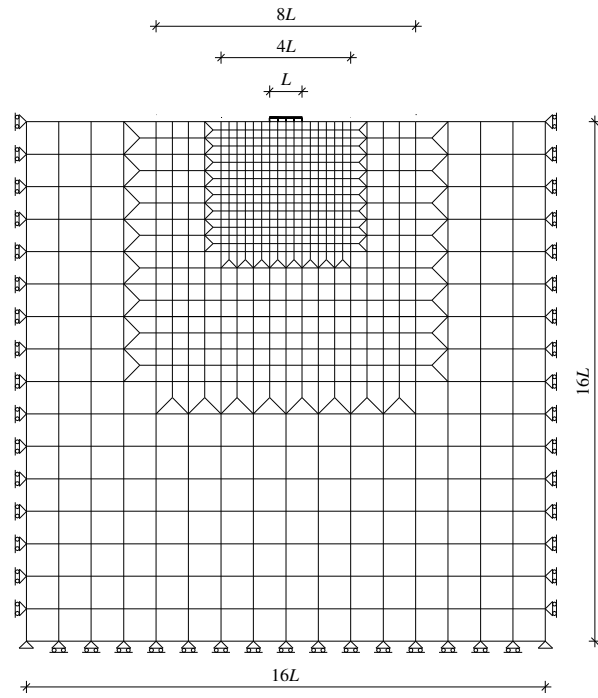


Fig. 11. Meshes adopted for the two-dimensional FE models with a foundation beam subdivided into 4 equal FEs. Models with mesh dimension  $8L$  (FEM 8L) (a) and  $16L$  (FEM 16L) (b).

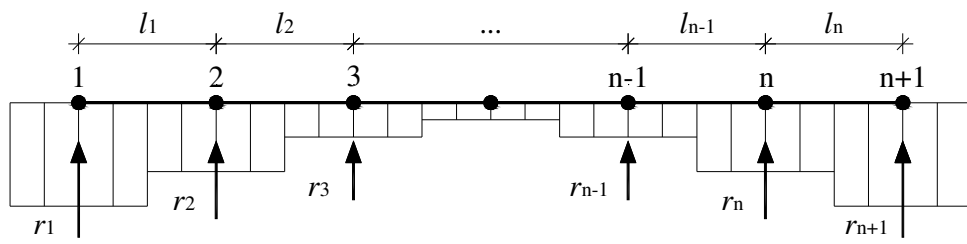


Fig 12. Piecewise constant pressure elements adopted in [17].

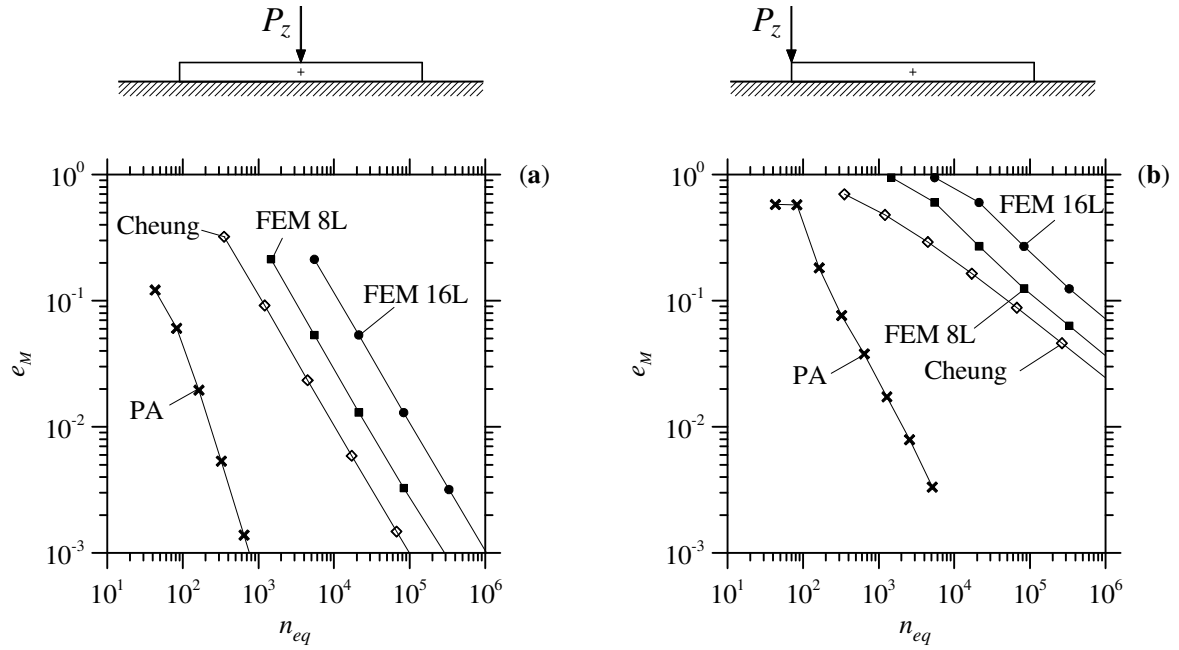


Fig. 13. Euler-Bernoulli beam ( $L/h=10$ ,  $\alpha L=20$ ) subjected to a vertical force  $P_z$  at midspan (a) and at one end section (b). Relative errors  $e_M = |M_{\max} - M_{\text{ref}}| / |M_{\text{ref}}|$  in terms of the maximum bending moment versus number of equation  $n_{eq}$  for the present analysis (PA), Cheung's solution [17] and meshes FEM 8L and FEM16L.

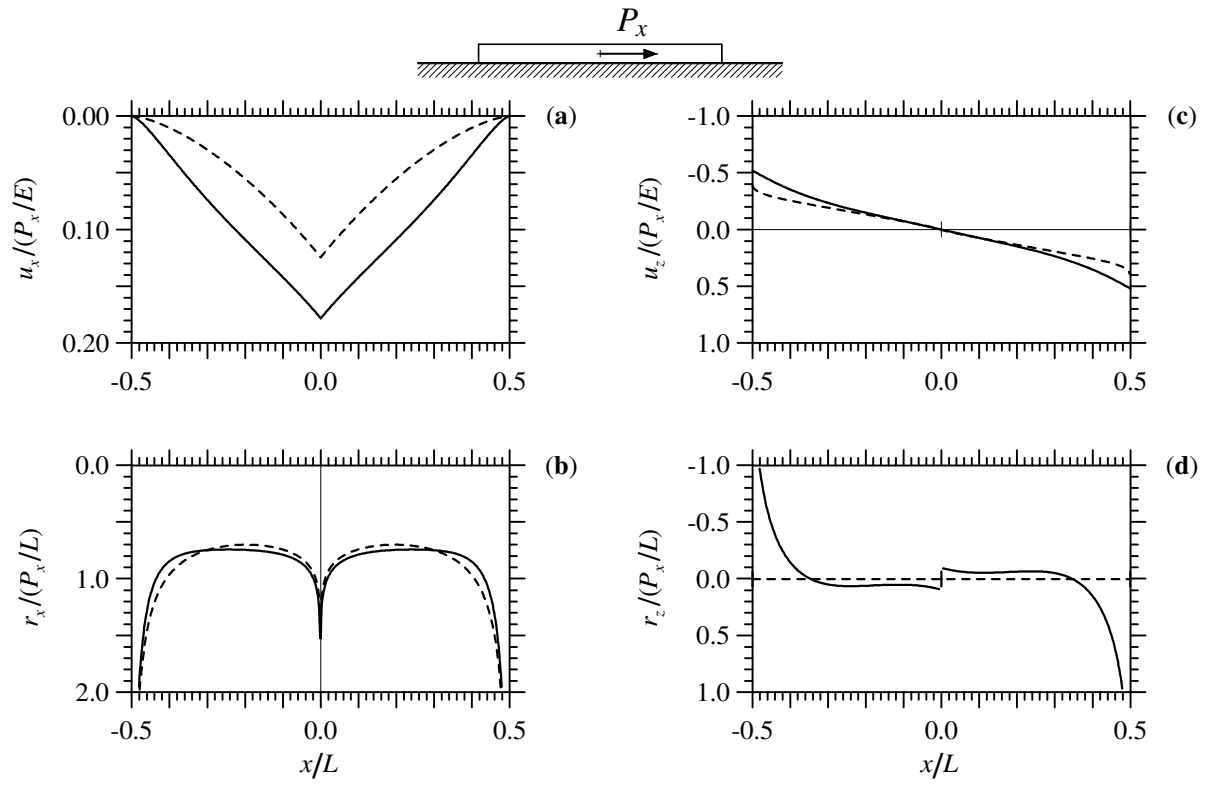


Fig. 14. Beam with  $L/h = 10$ ,  $\alpha L = 10$  (solid line) and thin coating with  $\beta L = 0.83$  (dashed line) in perfect adhesion to a half-plane, loaded by a horizontal point force  $P_x$  at midspan. Nondimensional values of  $u_x$  (a),  $r_x$  (b),  $u_z$  (c), and  $r_z$  (d) versus  $x/L$ .



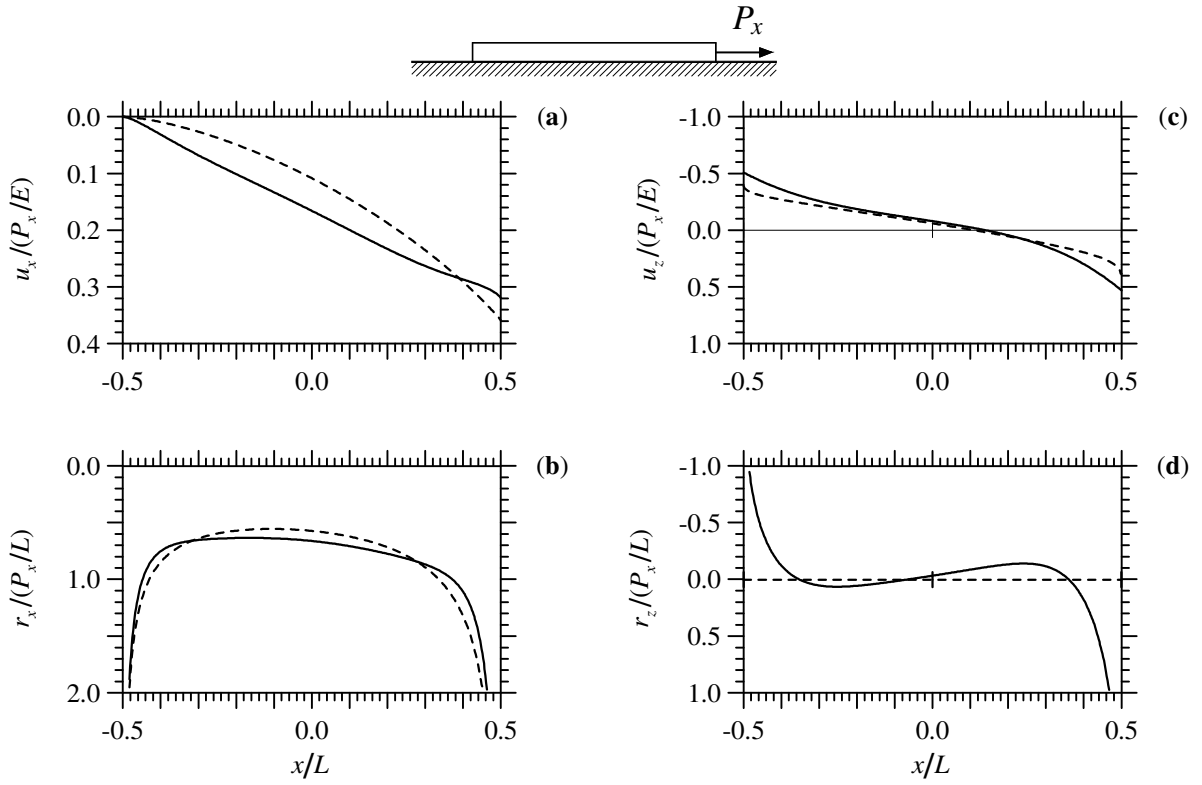


Fig. 15. Beam with  $L/h = 10$ ,  $\alpha L = 10$  (solid line) and thin coating with  $\beta L = 0.83$  (dashed line) in perfect adhesion to a half-plane, loaded by a horizontal point force  $P_x$  at one end section. Nondimensional values of  $u_x$  (a),  $r_x$  (b),  $u_z$  (c), and  $r_z$  (d) versus  $x/L$ .

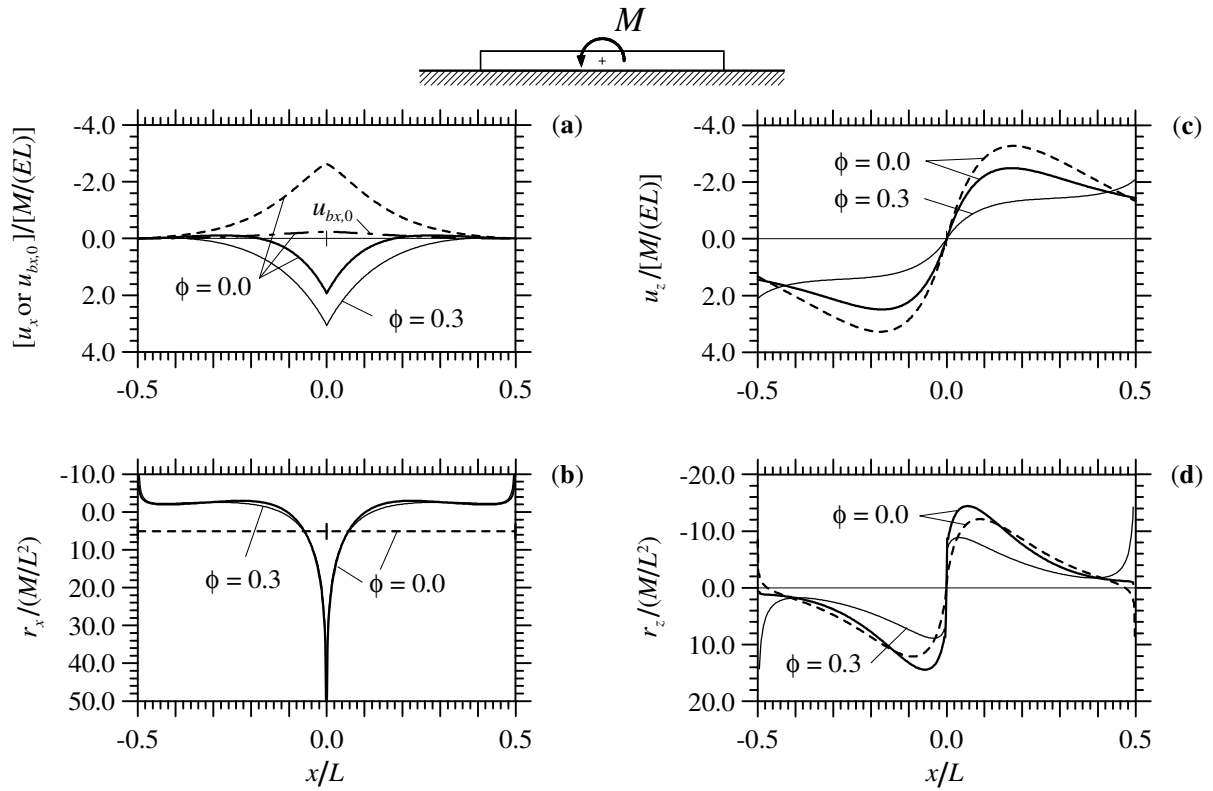


Fig. 16. Beam ( $L/h=10$ ,  $\alpha L=10$ ) loaded by a bending moment  $M$  at midspan. Nondimensional values of  $u_x$  (a),  $r_x$  (b),  $u_z$  (c), and  $r_z$  (d) versus  $x/L$  for perfect adhesion with  $\phi = 0.0$  and  $0.3$  (thick and thin solid line), and for frictionless contact with  $\phi = 0.0$  (dashed line). Horizontal displacement  $u_{bx,0}$  (dash-dot line in (a)) is referred to the centreline of the perfectly bonded beam with  $\phi = 0.0$ .

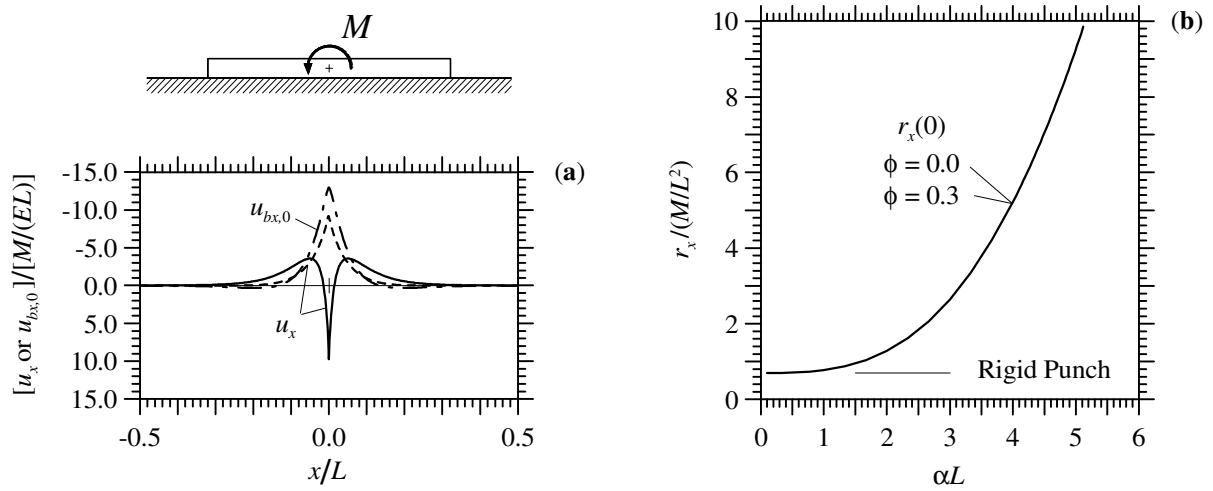


Fig. 17. Beam ( $L/h=10$ ) loaded by a bending moment  $M$  at midspan, comparison between perfect adhesion (solid line) and frictionless contact (dashed line). Nondimensional values of  $u_x$  versus  $x/L$  obtained for  $\alpha L=40$  and  $\phi = 0.0$  (a); and nondimensional values of  $r_x$  at midspan versus  $\alpha L$  obtained for  $\phi = 0.0$  and  $0.3$  (b). Horizontal displacement  $u_{bx,0}$  (dash-dot line in (a)) is referred to the beam centreline.

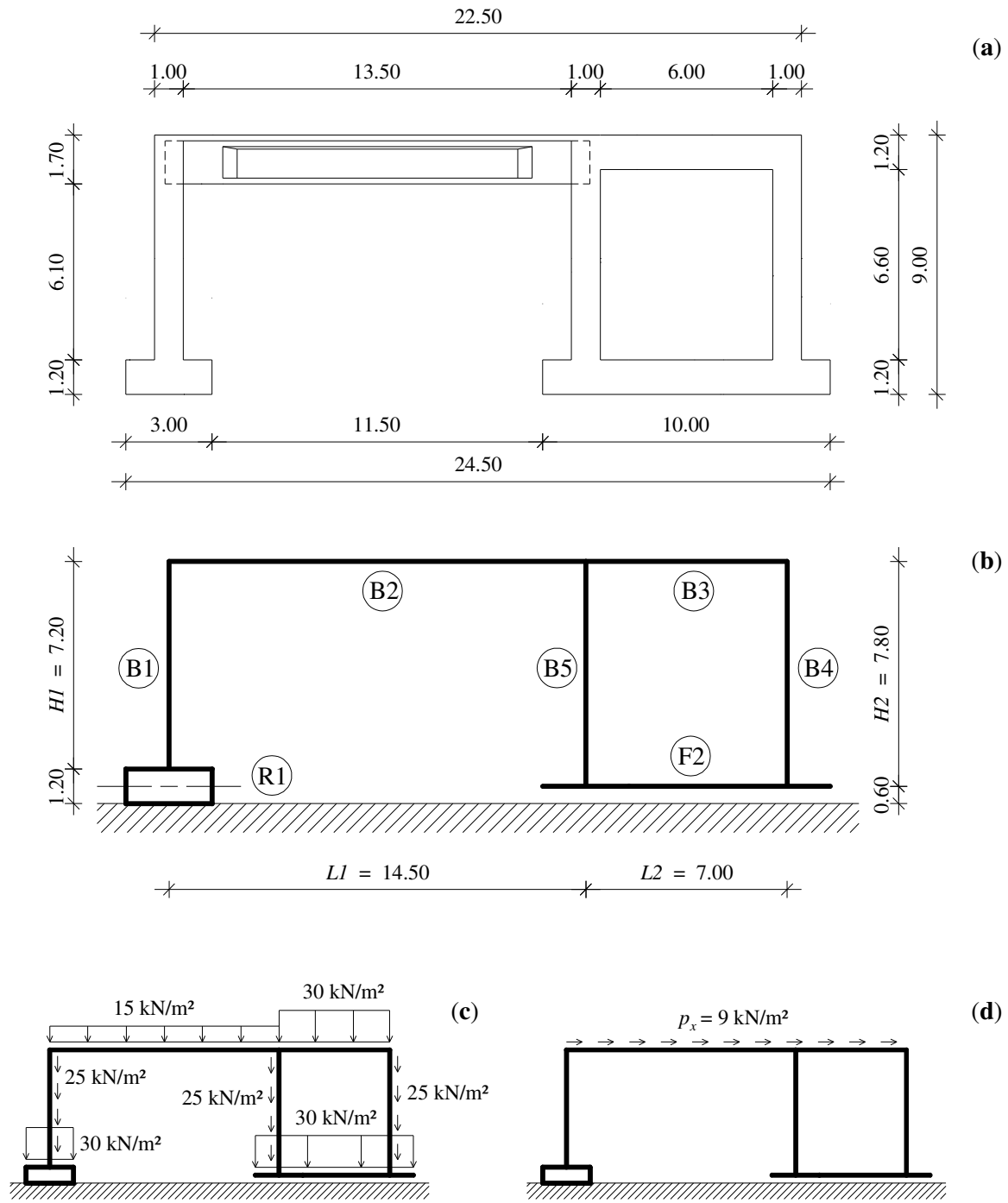


Fig. 18. Cross-section geometry of the double-cell tunnel investigated (a); corresponding two-bay frame analysed under plane strain assumption (b); and load cases considered (c, d).

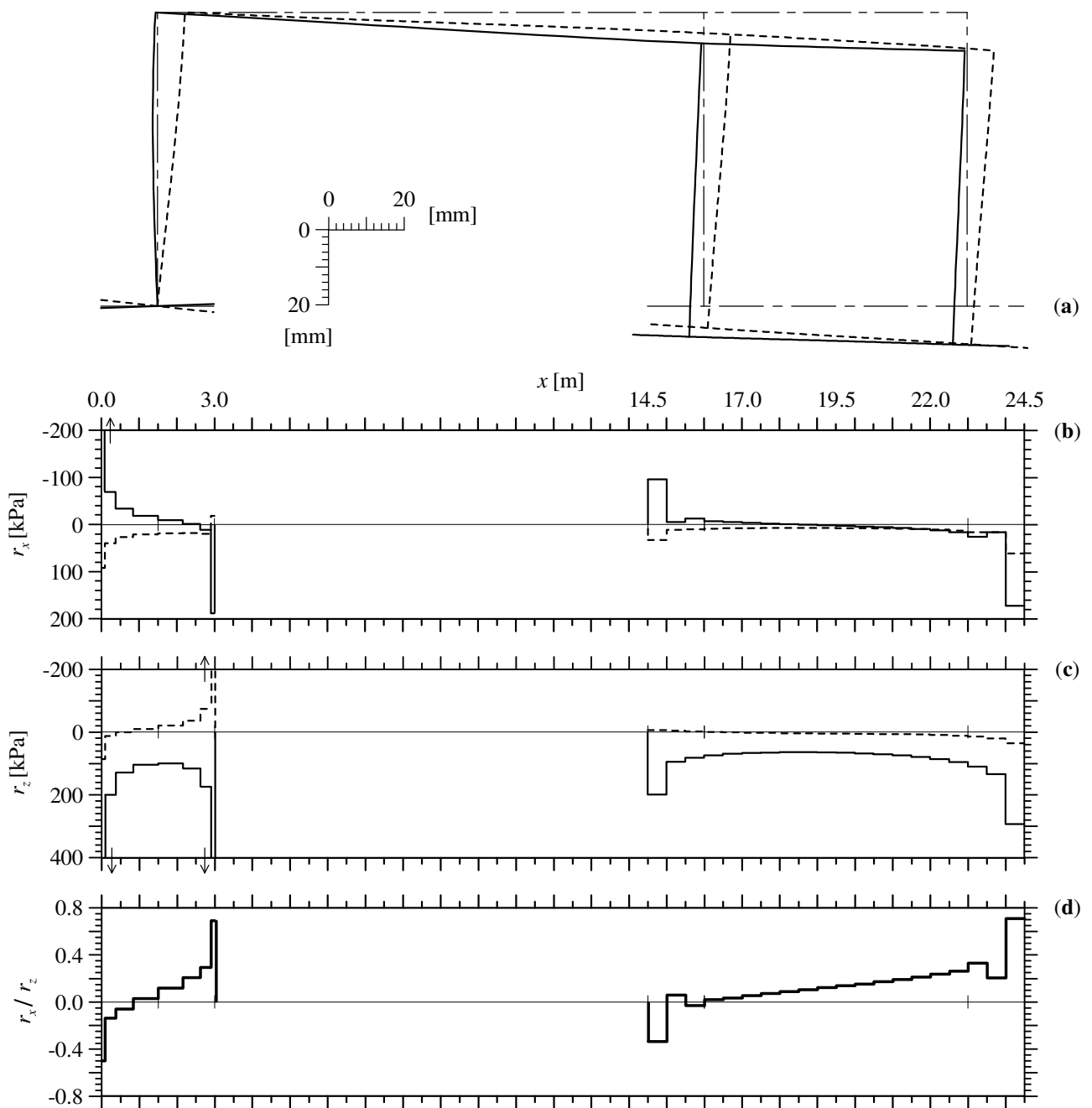


Fig. 19. Frame deflections (a) and reactions underneath rigid punch and foundation beam (b, c) for the structure subjected to self-weight (solid line) and lateral load (dashed line). Ratio  $r_x/r_z$  for the two load cases acting simultaneously (d). Dash-dot line in (a) represents the undeformed frame.

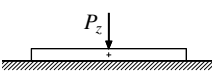
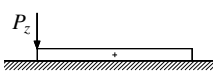
				
<b>Euler-Bernoulli</b>	<i>C</i>	$\lambda$	<i>C</i>	$\lambda$
PA	504	1.99	56	1.13
Cheung	124	1.02	16	0.47
FEM 8L	251	0.98	44	0.51
FEM 16L	1404	1.02	139	0.55
<b>Timoshenko</b>	<i>C</i>	$\lambda$	<i>C</i>	$\lambda$
PA	205	1.47	105	1.07
Cheung	217	0.76	16	0.40
FEM 8L	102	0.67	12	0.36
FEM 16L	77	0.58	17	0.34

Table 1. Euler-Bernoulli and Timoshenko ( $\phi = 0.3$ ) beams ( $L/h=10$ ,  $\alpha L=20$ ) subjected to a vertical force  $P_z$  at midspan and at one end section. Parameters of the convergence rate expression  $C n_{eq}^{-\lambda}$  for relative error  $e_M$  in terms of the maximum bending moment. Comparison between present analysis (PA), Cheung's solution [17] and two-dimensional FE models.